

Article

Petrographic Analysis of Mafic and Ultramafic Rocks in Northern Thailand: Implications for CO₂ Mineralization and Enhanced Rock Weathering Approach

Tadsuda Taksavasu 

Department of Mining and Petroleum Engineering, Faculty of Engineering, Chiang Mai University, 239 Huay Kaew Road, Suthep, Muang Chiang Mai 50200, Chiang Mai Province, Thailand; tadsuda.t@cmu.ac.th

Abstract: Mafic and ultramafic rocks have become a promising approach for atmospheric carbon dioxide (CO₂) reduction, as they are major sources of CO₂-reactive minerals, i.e., olivine, pyroxene, plagioclase, and serpentine. The minerals potentially sequester CO₂ by turning it into a stable solid phase through carbon mineralization in the rock weathering process. However, detailed descriptions and evaluations of the target formations are lacking. This study investigates the mineralogical composition and microtextural characteristics of representative mafic and ultramafic rocks observed in northern Thailand, using a petrographic analysis. The results show that variations in CO₂-reactive mineral assemblages of rocks certainly affect their theoretical CO₂ uptake potential. Ultramafic rocks tend to sequester larger amounts of CO₂ than mafic rocks. The microtextural observation reveals the mineral size ranges of 0.05–5 mm for ultramafic and mafic intrusive rocks and 0.01–2 mm for mafic extrusive and metamorphosed rocks. Reducing the rock size to be equal to the average size of the reactive minerals could be considered one of the practical designs in enhanced rock weathering activities. Understanding the mineralogical and textural characteristics of target rocks thus plays a crucial role in further georesource exploration and engineering designs, supporting climate action strategies on various scales.



Academic Editor: Maurizio Barbieri

Received: 22 January 2025

Revised: 23 February 2025

Accepted: 25 February 2025

Published: 1 March 2025

Citation: Taksavasu, T. Petrographic Analysis of Mafic and Ultramafic Rocks in Northern Thailand: Implications for CO₂ Mineralization and Enhanced Rock Weathering Approach. *Geosciences* **2025**, *15*, 89. <https://doi.org/10.3390/geosciences15030089>

Copyright: © 2025 by the author. Licensee MDPI, Basel, Switzerland. This article is an open access article distributed under the terms and conditions of the Creative Commons Attribution (CC BY) license (<https://creativecommons.org/licenses/by/4.0/>).

Keywords: carbon geological sequestration; climate action; CO₂ removal; emission reduction; igneous petrography; mineral size; mineralogy

1. Introduction

Cumulative carbon dioxide (CO₂) emissions from human activities drastically increase atmospheric CO₂ concentration and consequently induce global warming and ultimate climate change. Carbon Geological Sequestration (CGS) technology has been proposed for decades to mitigate the effects of climate change through atmospheric CO₂ removal and/or anthropogenic CO₂ emission reduction [1–10]. It refers to engineering processes in which the CO₂, captured from emitting sources or from the air is stored or sequestered in specific geological formations, whether at the surface, near surface, or subsurface. At least four CO₂ trapping mechanisms have been introduced, including structural/stratigraphic, capillary, solution, and mineral traps. Each mechanism has a discrete capacity, storing time, and storage security [8,11–13]. Their efficiencies also depend on the types of geological units and environmental conditions [14–18]. The mineral trap is currently considered to be the most stable permanent CO₂ storage as the CO₂ is turned into solid carbonate phases through a process called CO₂ mineralization [9,10,12,14,19–26]. Thus, understanding suitable geological formations for this approach is necessary.

One of the promising candidates for long-term carbon sequestration through CO₂ mineralization is mafic and ultramafic rock formations [8,10,14,20,27–31]. They have been known as igneous origins that are composed of relatively high contents (greater than 45%) of dark-colored silicate minerals, including olivine, pyroxene, plagioclase, and serpentine [32]. These minerals distinctly provide major sources of divalent cations, including magnesium, calcium, and iron. These cations are highly reactive to the molecules of CO₂ and consequently induce variable carbonate phase formations [8,19]. The chemical reactions between the minerals and CO₂ are spontaneous and exothermic, as they naturally occur during chemical weathering and alteration of the rock formations on geologic time scales [33–43]. It has previously been reported that nearly 1.1 Gt of atmospheric CO₂ is absorbed annually through the chemical rock weathering and alteration processes of the mafic and ultramafic rocks [7]. With a global mafic and ultramafic rock resource estimation, up to 60×10^6 Gt of atmospheric CO₂ could potentially be sequestered by these rocks [9]. However, the reaction rates are apparently slow in nature.

Over the past decades, an enhanced rock weathering (ERW) technique has been proposed as one of the most promising engineering approaches to accelerate the CO₂ mineralization rates of target rocks [26,44–49]. It simply involves processes of grinding the rocks into finely grained powders and spreading them on lands, coasts, or oceans [34,50–56]. The size reduction significantly increases the surface areas of the rock-forming minerals, hence inducing chemical reactions with CO₂ in the air or water. Ultramafic and mafic rocks, mine tailings, and industrial waste with high contents of divalent cations and/or alkali elements have certainly been considered potential materials for ERW [26,48,49,54,57–60]. Besides the suitable composition, an understanding of textural characteristics, especially of any natural rocks, distinctly supports an optimal grain-size selection used for the ERW strategy [55,61]. Despite its several challenges, including operating processes, cost, unexpected pollution or hazard, and resource availability, the development of early-stage exploration techniques is certainly a worthy step for ERW.

This study focuses on an investigation of representative mafic and ultramafic rocks observed in the north of Thailand to support ERW technology against climate change. Standard petrographic details of those rocks have initially been documented, including mineral assemblages, textural characteristics, and deformed-to-altered features. The mineral contents and descriptions of the rocks positively provide an insight to primarily assess their potential CO₂ uptake by mineral traps. Observation of the rock's mineralogical and textural characteristics is crucial for a particular georesource exploration and further development of engineering or mining designs for alternative carbon sequestration plants.

2. Geological Background

The mafic and ultramafic igneous rocks involved in this study consist of DCv, Cb, CPu, PTrv, and bs units occurring along a major part of the Sukhothai Fold Belt, SE Asia, and covering six provinces in the north of Thailand as shown in Figure 1. The geologic ages of these units range from the middle Paleozoic to Cenozoic Era, including Devonian-Carboniferous (DCv), Carboniferous (Cb), Carboniferous–Permian (CPu), and Permian–Triassic (PTrv), and Quaternary (bs). The ultramafic units, including DCv, Cb, and CPu, have been described as parts of the Chiang Rai–Chiang Mai Volcanic Belt [62–66] and the Pha Som Ultramafic Belt [63]. The rocks are certainly composed of peridotite, pyroxenite, and/or serpentinite, in association with gabbro, multi-stage volcanic rocks, and sedimentary rocks, i.e., limestone, sandstone, and shale, formed in the relevant ages. The ultramafic rocks of these units were originally formed by crystallization of deep-seat magmas underneath the paleosurface. The emergence of the rocks in DCv, Cb, and CPu units has been interpreted as a result of oceanic crust subductions and subsequent plate collisions [63,64]. Regional metamorphism

and deformation of the rocks in these units forming metabasites and low-to-medium-grade metamorphic rocks are common, especially in the *Cb* unit. On the other hand, *PTrv* and *bs* units represent mafic volcanic rocks formed in the pre-Cenozoic and Cenozoic ages, respectively [63]. The *PTrv* unit comprises pyroclastic rocks associated with gabbro, diabase, and andesite, whereas the rocks of the *bs* unit are predominantly basalts. Both units have been previously interpreted as formed by numerous volcanic activities, including various-degree eruptions and lava flows [62,63]. Remnant volcanoes with basaltic composition aligned in a north–south direction are still observed as representing the *bs* unit.

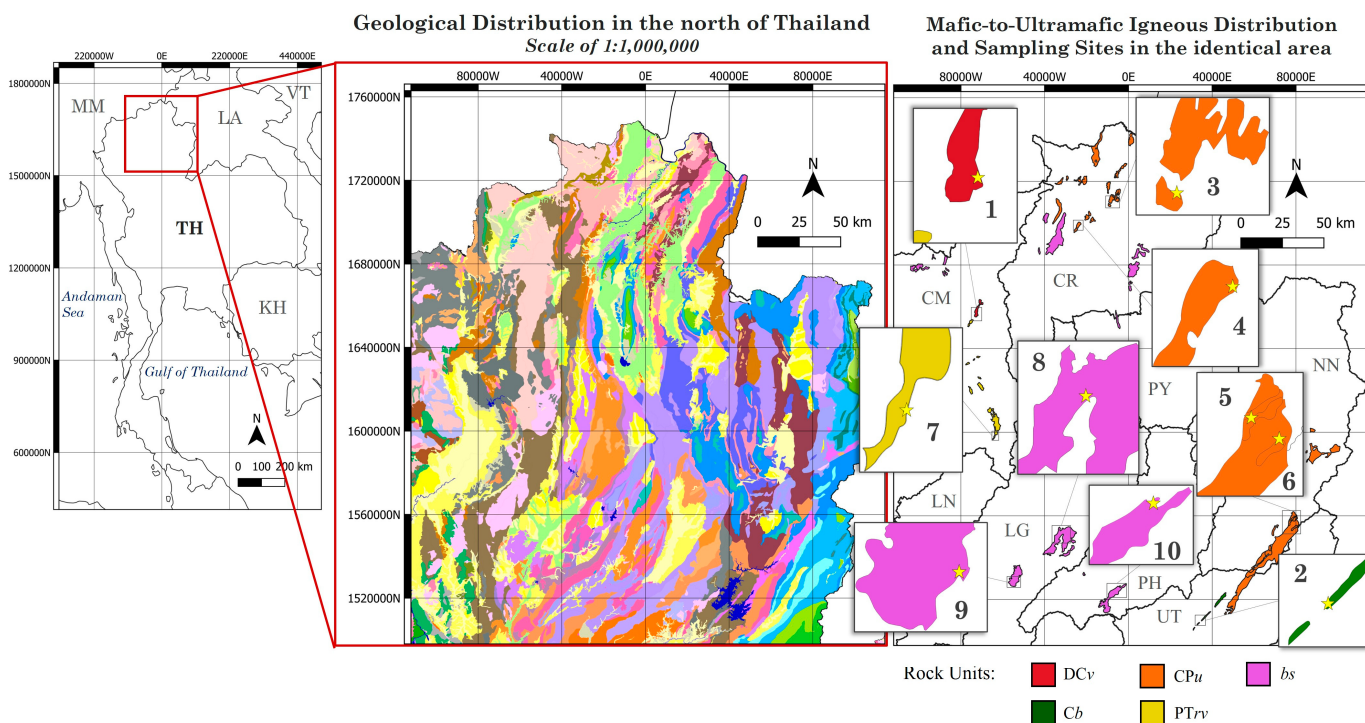


Figure 1. Geologic maps of the northern region of Thailand in scales of 1:1,000,000 showing the overall north–south directional fold belts and the distribution of mafic and ultramafic igneous rock units in the area. The maps have been adapted from DMR (2014) [67], Bandibas and Takarada (2019) [66], and Promneewat et al. (2022) [68]. Ten sampling sites of this work are indicated by yellow stars. Each number indicates a sample name, including 1 = Phrao; 2 = Pha Luat; 3 = Mae Chan; 4 = Mae Fah Luang; 5 = Huay Lao; 6 = Na Noi; 7 = Mae On; 8 = Mae Tha; 9 = Sobprab; 10 = Den Chai. More detailed descriptions of the map legends can be found on the open-source site [69]. CM = Chiang Mai, CR = Chiang Rai, KH = Cambodia, LA = Laos, LG = Lampang, LN = Lamphun, MM = Myanmar, NN = Nan, PH = Phrae, PY = Phayao, TH = Thailand, UT = Uttaradit, VT = Vietnam.

3. Materials and Methods

3.1. Rock Sampling and Lithologic Descriptions

Representative mafic and ultramafic rock samples used in this study were collected from the formerly known igneous outcrops observed in six provinces of the northern region of Thailand, including Chiang Mai, Chiang Rai, Lampang, Nan, Phrae, and Uttaradit (Table 1). Lithological features, in terms of textures, colors, mineralogy, and crystal sizes, were briefly determined in the field and laboratory. All samples exhibit dark-colored microcrystalline-to-crystalline rocks (Figure 2). The colors of fresh rocks include black, dark gray, reddish brown, greenish black, greenish gray, and dark green. Some of them distinctly show porous (vesicular) textures, whereas some samples exhibit deformation (foliated) features. Pyroclastic textures were also observed in only one sample.

Based on lithological characteristics, the rock types were temporarily classified as shown in Table 1.

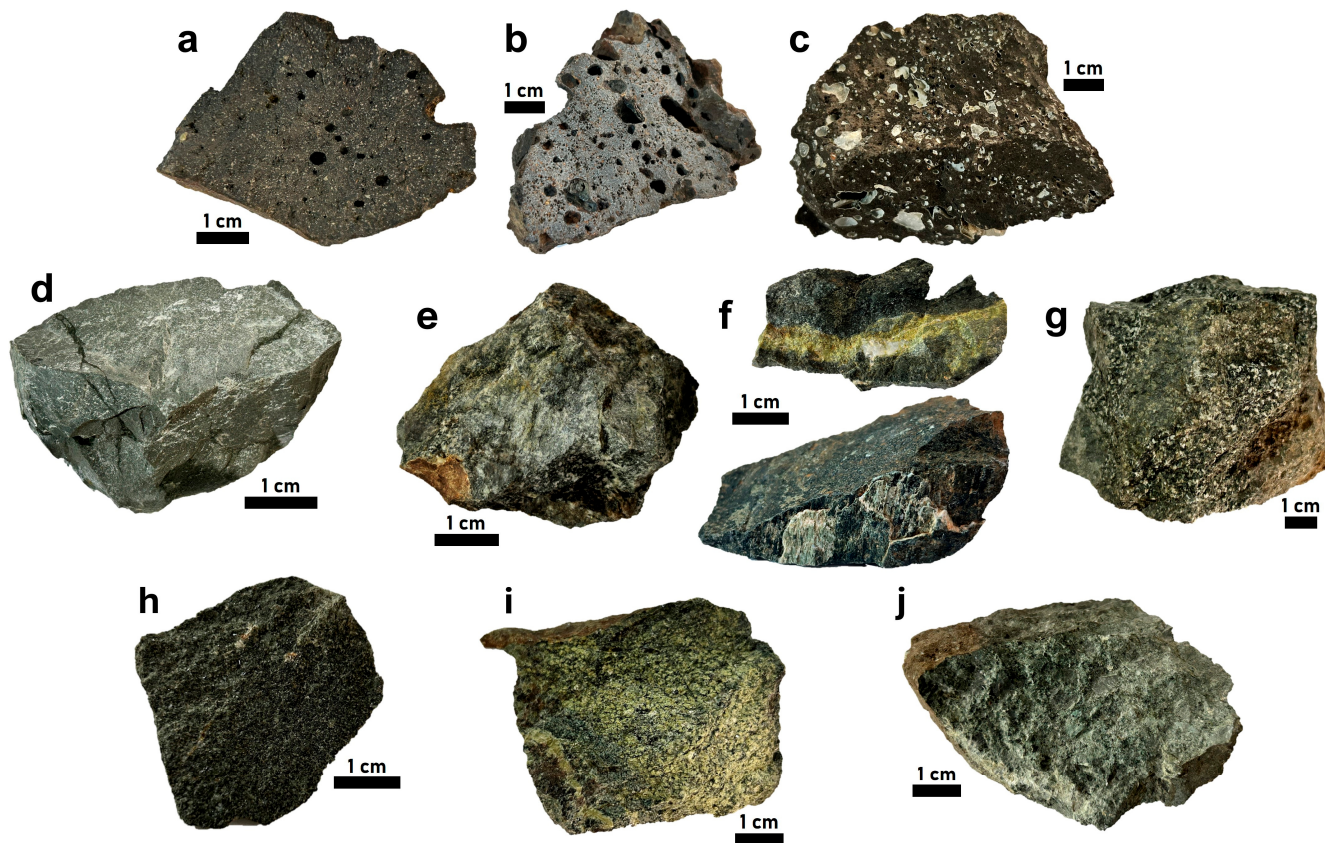


Figure 2. Lithological characteristics of the studied specimens exhibit dark-colored crystalline-to-vesicular textures, indicating mafic and ultramafic compositions. Some specimens show metamorphic features. The specimens come from (a) Mae Tha; (b) Sobprab; (c) Den Chai; (d) Mae Chan; (e) Pha Luat; (f) Mae Fah Laung; (g) Na Noi; (h) Phrao; (i) Hauy Lao; (j) Mae On.

Table 1. Details of the sampling locations, WGS 84 coordinates (*Mercator 41*), rock units, and brief lithologic description.

Rock Unit	Sample Site [Sample No.]	Province	Latitude	Longitude	Lithologic Description
DCv	Phrao [1]	Chiang Mai	1,656,777.346 N	71,786.47703 W	Black to greenish-black, Dense, Phaneritic-to-cumulated texture; Ol, Px
Cb	Pha Luat [2]	Uttaradit	1,502,454.345 N	30,388.22661 E	Greenish gray, pale gray, yellowish brown, Phaneritic texture with low-grade deformed (foliated) features; Crosscut by Chl-Qz veins
CPu	Mae Chan [3]	Chiang Rai	1,721,148.906 N	5085.97194 E	Dark green to dark gray, Phaneritic texture; Pl, Px
CPu	Mae Fah Luang [4]	Chiang Rai	1,709,346.880 N	8392.25100 W	Dark gray, greenish black, and pale green, Phaneritic texture with low-grade deformed (schistose) features; Crosscut by Cal-Ep veins

Table 1. Cont.

Rock Unit	Sample Site [Sample No.]	Province	Latitude	Longitude	Lithologic Description
CPu	Huay Lao [5]	Nan	1,557,746.874 N	77,298.03278 E	Greenish black-to-green, Phaneritic texture with weakly foliated features, high-degree alteration; Srp, Px
CPu	Na Noi [6]	Nan	1,554,609.250 N	80,359.61868 E	Greenish gray to dark gray, Phaneritic texture with low-grade deformed (weakly foliated to schistose) features; Crosscut by Chl-Qz veinlets
PTrv	Mae On [7]	Chiang Mai	1,598,001.988 N	63,354.72923 W	Dark green to pale green, Medium-to-fine-grained pyroclastic texture; volcanic fragments
bs	Mae Tha [8]	Lampang	1,553,343.767 N	30,707.00548 W	Dark gray to black, Porphyritic-vesicular texture; Ol, Px phenocrysts, Px, Pl groundmass; 1–2 mm vesicles
bs	Sobprab [9]	Lampang	1,535,108.371 N	54,232.37178 W	Dark gray-to-reddish brown, Aphanitic-to-glassy vesicular texture; Ol, Px, Pl; 1–5 mm vesicles
bs	Den Chai [10]	Phrae	1,526,421.533 N	5843.656028 W	Black to dark gray, Aphanitic-to-glassy vesicular texture; vesicles are filled with white Ze, Cal; 1–2 mm vesicles

Abbreviation: Cal = calcite, Chl = chlorite, Ep = epidote, Ol = olivine, Pl = plagioclase, Px = pyroxene, Qz = quartz, Srp = serpentine, Zeo = zeolite.

3.2. Sample Preparation and Optical Mineral Analysis

The selected rock samples were prepared as standard petrographic thin sections by a commercial lab. Fourteen single-polished thin sections having the dimensions of 26 mm × 46 mm with 30-micron thickness were individually analyzed for their mineralogy and textural characterization using a Nikon Eclipse Ci-POL polarizing microscope at a magnification of 4× and 10×. Micrograph images of all observed features were carefully obtained under plane-polarized and cross-polarized light using a Nikon DS-Fi3 microscope camera with NIS-Elements imaging software Version 4.60. Mineral identification is based on the optical properties (opacity, relief, extinction, pleochroism, birefringence) and crystal habits of those rock-forming minerals. Crystal sizes, deformation features, alteration products, and degree of alteration, as well as textural relationships among the minerals and the order of crystallization in the rocks, were also described.

3.3. Modal Analyses

Quantitative mineralogical interpretations of all samples were performed through a point-counting method on thin sections. Each thin section was held on the rotatable stage of the microscope using slide clamps. Each identified mineral was counted in a grid intersection with a constant interval (1 mm) between two points in a row using an attached vernier scale. At least four hundred points were counted in each thin section. The ratio between the counting number of points representing a given mineral and the total number of points was normalized to 100%, indicating the modal percentage of that mineral. The

mineral contents of the samples obtained by this method were considered to identify the rock names based on the International Union of Geological Sciences (IUGS) standards [32].

In addition, X-ray diffraction (XRD) analysis was conducted at the commercial lab to identify the mineral phases blended in the samples (i.e., plagioclase series, opaques, clays). The remaining rock samples were individually ground to powder using a mortar and pestle. The obtained powder samples were analyzed using a Bruker D8 Advance diffractometer instrument with CuK α radiation. The accelerating voltage was 40 kV, and the filament current was 30 mA. The X-ray wavelength of 1.54 Å was used. XRD data were collected over the scan field of 2–70° 2θ with a step width of 0.04° 2θ and 1 s/step. Mineral phases in the samples were identified and quantified using the DIFFRACplus Eva Version 12.0 software with the reference XRD peak pattern database provided by the International Centre for Diffraction Data (ICDD).

4. Results

Based on petrographic observation and modal analysis, the studied rock samples can be divided into six groups, including vesicular olivine basalt, gabbro, metabasite, peridotite, altered pyroxenite, and basaltic tuff. Each group represents discrete mineral contents, unique microtextural characteristics, and crystal size ranges, as provided in the following sections.

4.1. Vesicular Olivine Basalt

All samples retrieved from the rock unit *bs* are classified as basaltic rocks as they distinctly exhibit abundances of primary mafic minerals, including olivine, plagioclase, and clinopyroxene (augite), with significant amounts of opaque iron–titanium oxide minerals. Olivine contents of the samples collected from Den Chai and Sobprab are equal (10.63 modal%), whereas those of Mae Tha are approximately 8.71 modal%. The modal percentages of plagioclase are 50, 41.03, and 38 for Den Chai, Mae Tha, and Sobprab, respectively. The augite in the same sample set, on the other hand, has modal percentages of 20.25, 12.31, and 14.13, respectively. Secondary-phase minerals include chlorite, smectite, iron–titanium oxide, zeolite, and carbonate. Zeolite and calcite are locally observed as vesicle-filling minerals or amygdules in the Den Chai and Mae Tha samples, whereas the concentric thin layers of iron oxides are found filling in the vugs of the Sobprab samples.

Microporphyritic textures are entirely observed under the microscopic views, comprising microphenocrysts (sizes of 0.1–1.2 mm) and groundmass (less than 0.1 mm). Microphenocrysts are found to be euhedral-to-subhedral olivine, clinopyroxene, and plagioclase surrounded by subhedral-to-anhedral plagioclase and clinopyroxene groundmass (Figure 3a,b). The accumulation of microphenocrysts forming glomerocrysts (single mineral type) and cumulocrysts (multiple mineral types) is commonly observed. The grain/crystal boundaries of the microphenocrysts mostly show irregular corrosion features (embayed) (Figure 3c). Moreover, anhedral olivine, isotropic volcanic glass, and equant-to-stubby opaque minerals are also observed in the groundmass of the Mae Tha and Sobprab basalts. Trachytic textures are particularly found in the basaltic samples from Den Chai, indicating near-parallel arrangements of tabular-shaped plagioclase crystals within the groundmass (Figure 3d).

Olivine in all basaltic samples ranges from 0.05 to 1.0 mm in diameter and significantly shows a moderate-to-extreme degree of alteration. The olivine crystals are fully-to-partially replaced by reddish-brown iddingsites, a mixture of relict olivine, iron oxides, and clay minerals, observed under plane- and cross-polarized light. Some olivine grains in the Sobprab basalts are locally altered to smectites and/or talc.

Plagioclase certainly forms in prismatic-to-tabular shapes having sizes of 0.01–0.4 mm. Polysynthetic twins are widely observed. Some crystals exhibit swallow-tail textures

indicating quench crystallization. The alteration levels of plagioclases are low (less than 10%) in Mae Tha and Sobprab samples and low-to-medium (less than 10–70%) in Den Chai samples. The alteration products are found to be sericite and clay minerals.

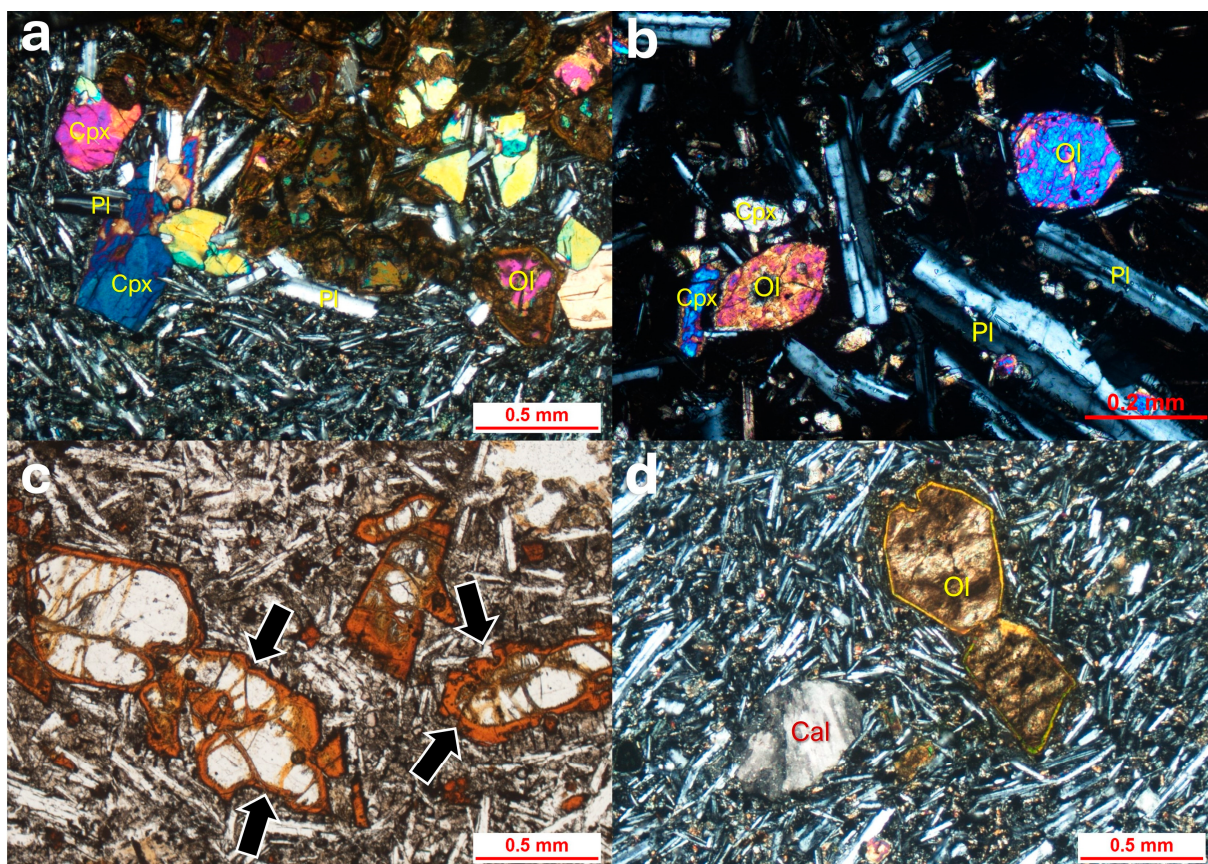


Figure 3. Photomicrographs of vesicular olivine basalts collected from the rock unit *bs* showing microporphyritic and trachytic textures associated with low-to-moderate alteration levels of primary minerals: (a) Cumulocrysts consisting of altered olivine (Ol), clinopyroxene (Cpx), and plagioclase (Pl) crystals surrounded by plagioclase/pyroxene groundmass, taken from Den Chai sample under cross-polarized light. (b) Olivine and plagioclase microphenocrysts surrounded by plagioclase/pyroxene groundmass are present at higher magnification of Mae Tha sample taken cross-polarized light. The olivine shows barely altered to secondary products; (c) Olivine glomerocrysts observed under the plane-polarized light of Sobprab sample exhibiting irregular embayed crystal outlines (arrows). Reddish brown-colored iddingsites are commonly present along the rims of the crystals as a result of olivine alteration; (d) Subparallel arrangement of plagioclase crystals displaying trachytic textures and surrounding fully altered olivine grains observed under cross-polarized light of Den Chai sample. Calcite (Cal) is also present as amygdale minerals filling in the vesicle.

Augite has a size range of 0.01–0.4 mm. It exhibits short-prismatic, pale brown crystals associated with nearly 90° of cleavages and inclined extinction. No alteration phase of augite is observed.

Opaque minerals of these samples are likely considered as iron–titanium oxides (ilmenite?) forming skeleton-to-equant shapes with sizes of less than 0.1 mm. The alteration products, especially leucoxene, are barely observed throughout the samples suggesting low-degree alteration.

4.2. Gabbro

The samples representing the rock unit *CP_u*, which were collected from Mae Chan, are classified as gabbroic rocks. The mineral assemblages are predominantly plagioclase,

amphibole (hornblende), clinopyroxene, and orthopyroxene, with minor amounts of olivine and opaque iron–titanium oxide minerals. Based on the relative mafic mineral contents and percentage of plagioclase, two end members have been determined from the gabbroic samples, including pyroxene–hornblende gabbronorite and gabbronorite.

The pyroxene–hornblende gabbronorite primarily consists of 29.25 modal% plagioclase, 28.25 modal% hornblende, 21.25 modal% clinopyroxene, and 17.75 modal% orthopyroxene with limited contents of olivine (1.0 modal%) and opaque iron–titanium oxides (0.75 modal%). The observed secondary mineral phases (1.75 modal%) are chlorite, prehnite, and sericite. Microscopically, this sample exhibits a heteradcumulate (poikilitic) texture that comprises oikocrysts (up to 5 mm in size) of orthopyroxene and hornblende enclosing chadacrysts (0.05–1.5 mm in size) of plagioclase, clinopyroxene, and olivine (Figure 4a,b). Orthopyroxene oikocrysts are anhedral and embayed in shape, displaying pale pink to colorlessness. Some grains are observed as inclusions in hornblende due to the resorption. This mineral is altered to bowlingite (a fine-grained aggregate of smectite, chlorite, silica, serpentine, and talc) and serpentine/chlorite with a low-to-moderate degree (30–50%). Hornblende oikocrysts are anhedral with weakly pleochroic colors of pale yellow-yellowish brown-bluish green. Some hornblende crystals are formed as alteration products of clinopyroxene exhibiting mottled textures (Figure 4b). Plagioclase, which is 0.05–1.1 mm, distinctly exhibits euhedral crystals hosted by large orthopyroxene and subhedral crystals hosted by hornblende associated with embayed features. The alteration of plagioclase to sericite is estimated at low-to-moderate levels (30–50%). Clinopyroxene (sizes of 0.08–1.5 mm) forms euhedral-to-subhedral prismatic colorless crystals. It shows identical textural relationships and the alteration levels to the plagioclase. However, the clinopyroxene hosted by the orthopyroxene shows no alteration feature, while those hosted by the hornblende are moderately altered to amphibole. Anhedral and embayed olivine chadacrysts (up to 0.6 mm in size) are found in the orthopyroxene. The crystals show a very low degree of alteration to opaque minerals. Additionally, the intercumulus of this sample is locally found to be opaque iron–titanium oxides exhibiting up to 0.5 mm anhedral crystals formed in between the clinopyroxene grains.

The gabbronorite, on the other hand, is composed of a relatively high content of plagioclase (54.75 modal%) with 17.25 modal% clinopyroxene, 11.5 modal% opaque minerals, 6.0 modal% orthopyroxene, and 3.25 modal% olivine. The secondary phases include amphibole (3.75 modal%) and chlorite (3.5 modal%). The sample exhibits a cumulus texture comprising cumulus crystals of plagioclase, clinopyroxene, orthopyroxene, and olivine, and intercumulus minerals, including clinopyroxene and opaque iron–titanium oxides (Figure 4c). Plagioclase exhibits a euhedral-to-subhedral prismatic form with polysynthetic and simple twins. The crystal sizes range from 0.1 to 1.0 mm. Their alteration degree and products are similar to the plagioclase in the pyroxene–hornblende gabbronorite. Clinopyroxene crystals formed as cumulus and intercumulus crystals are subhedral-to-anhedral displaying weakly pale pink-colorless pleochroism. The average crystal size is 0.5 mm. Moderate alteration (30–50%) and replacement of the clinopyroxene by amphibole are particularly observed in the cumulus crystals. Orthopyroxene pseudomorphs exhibiting anhedral-to-subhedral short prismatic forms (up to 0.8 mm in diameter) are completely replaced by pale green amphibole (uralite). Distinctive pyroxene cleavages are well preserved. Pseudomorphs of pale green chlorite and opaque iron oxides after olivine are locally observed, having sizes of up to 0.6 mm. The intercumulus opaque minerals (sizes of 0.05–0.4 mm) are found among clinopyroxene crystals, showing corona features, as they are encrusted by brown secondary amphibole (Figure 4d). In addition, chloritic veinlets and invasive chlorite are locally observed as secondary minerals and alteration products of olivine.

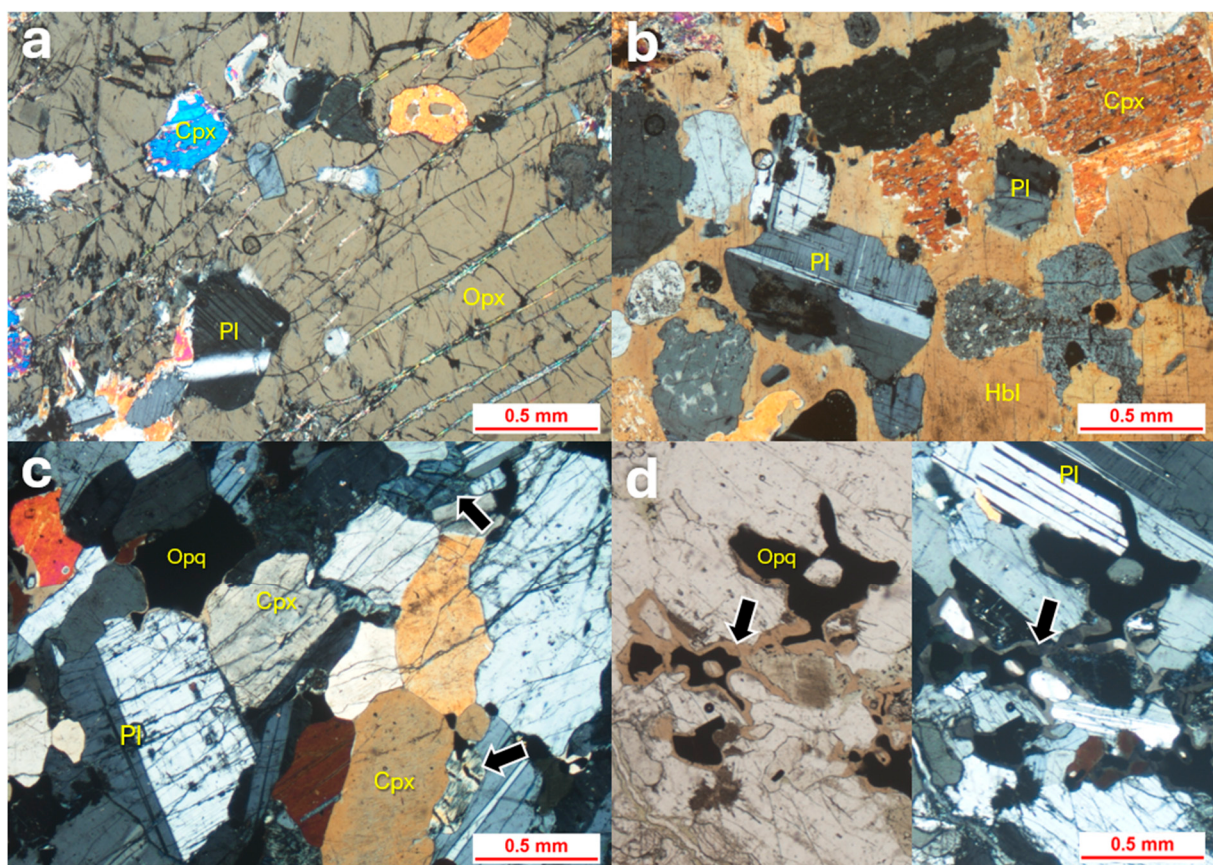


Figure 4. Photomicrographs of gabbros collected from Mae Chan representing the rock unit *CP_u*. Based on major mineral assemblages, the samples can be divided into two subtypes, including pyroxene–hornblende gabbronorite (**a,b**) and gabbronorite (**c,d**). (**a**) Poikilitic texture exhibiting plagioclase (Pl) and clinopyroxene (Cpx) chadacrysts hosted by large orthopyroxene (Opx) oikocrysts that were taken under cross-polarized light. The chadacrysts are subhedral and lack alteration features. (**b**) Plagioclase and clinopyroxene chadacrysts hosted by hornblende (Hbl) oikocrysts are observed under cross-polarized light. Mottled textures can also be found in the clinopyroxene grains. (**c**) Cumulus texture comprising cumulus crystals of plagioclase and clinopyroxene, and intercumulus opaque minerals (Opq) observed under cross-polarized light. Former olivine and orthopyroxene are indicated by arrows resulting from the primary mineral alteration to chlorite. (**d**) Corona textures of the intercumulus opaque minerals are present both under plane- and cross-polarized light. The minerals are encrusted by pale-brown amphibole, which are indicated by arrows.

4.3. Metabasite

This group evidently represents metamorphosed versions of the mafic protoliths, including the sample from the rock unit *C_b* (collected from Pha Luat) and the samples collected from Mae Fah Luang and Na Noi, which are both representatives of the rock unit *CP_u*. All samples are abundant in amphibole (tremolite–actinolite?) and mineral pseudomorphs after clinopyroxene and plagioclase. Chlorite, epidote, opaque iron oxides, sericite, and quartz are common. Amphibole contents in the samples from Pha Luet and Mae Fah Luang are 45.25 and 67 modal%, respectively. Clinopyroxene is observed as 42.25 modal% in the Na Noi sample. Only the sample from Pha Luat contains moderately altered plagioclase (45.25 modal%), whereas the pseudomorphs of epidote, sericite, clay minerals, and opaque minerals after plagioclase likely occur in other samples. The modal percentage of epidote-group minerals varies in all samples as 3.25 (Pha Luat), 13.5 (Mae Fah Luang), and 17.5 (Na Noi). Chlorite is found in the samples from Pha Luat (3 modal%) and Na Noi (9 modal%), whereas quartz is observed in all samples ranging from 0.25 to 9.5 modal%.

Opaque minerals of this rock type are found in a range of 0.75–3.5 modal%. Carbonate minerals (1 modal%) are locally observed only in the sample from Mae Fah Luang.

According to metamorphic textural terminology, the samples microscopically exhibit granoblastic textures comprising coarse grains of altered clinopyroxene, plagioclase, and/or their pseudomorphs, and opaque minerals (Figure 5a,b). Nematoblastic foliations are observed in Pha Luat and Mae Fah Luang samples, displaying abundant linear fabrics of elongate, prismatic amphibole, and plagioclase (Figure 5c,d). All samples are crosscut by secondary-phase veinlets of epidote, chlorite, opaque minerals, quartz, and carbonates. In addition, the mineral assemblages and textural characteristics typically indicate a greenschist facies.

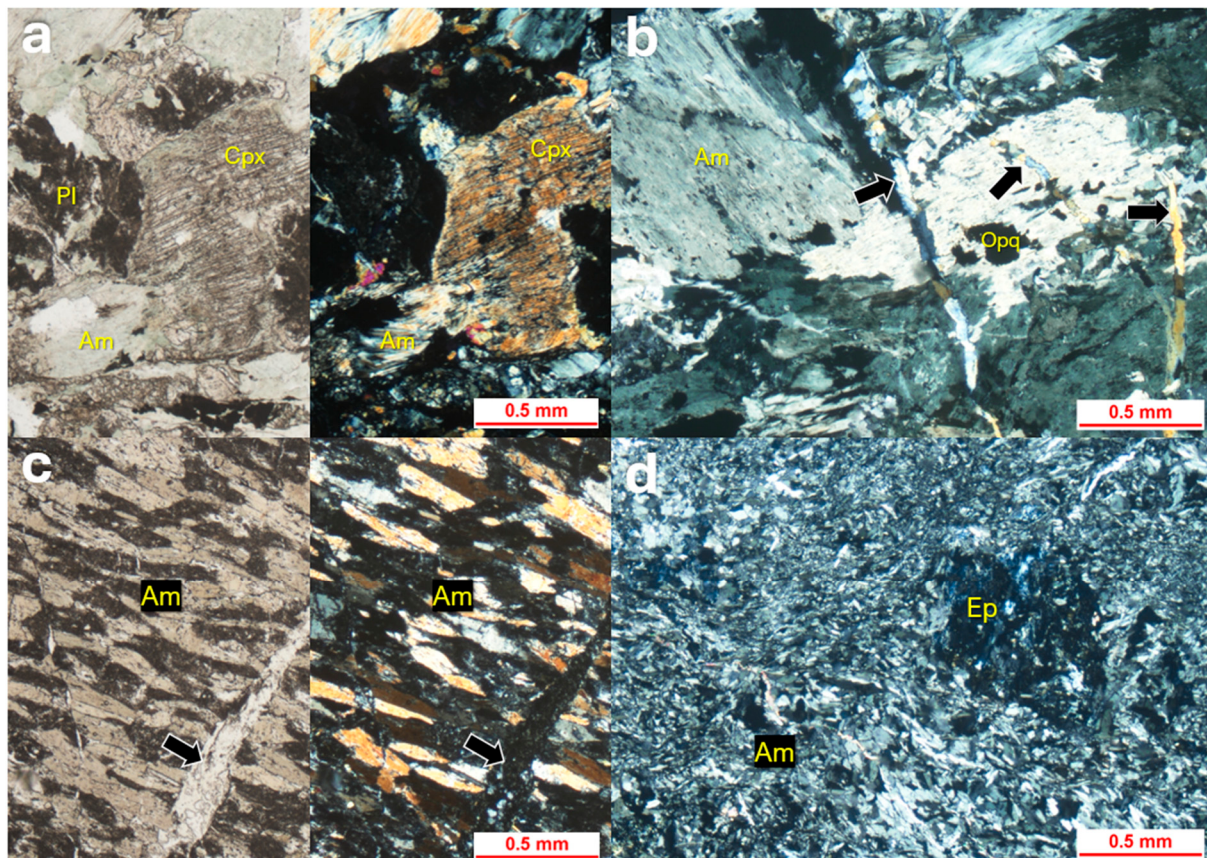


Figure 5. Photomicrographs of metabasites collected from the rock unit CP μ and C ν showing granoblastic and nematoblastic textures of mafic protoliths: (a) Granoblastic texture observed in the sample from Na Noi exhibiting coarse-grained clinopyroxene (Cpx) and plagioclase (Pl) under PPL and XPL. The clinopyroxene is altering to amphibole (Am) forming fibrous structures, whereas the plagioclase is fully replaced by clays, sericite, and opaque minerals. (b) Epidote veinlets (arrows) are present under cross-polarized light. The veinlets crosscut the granoblastic (amphibole) textures of Mae Fah Luang sample. (c) Nematoblastic texture comprising prismatic amphibole crystals formed in parallel orientation is shown in both PPL and XPL. Epidote-chlorite-opaque veinlet crosscut the sample is indicated by arrows. The sample comes from Pha Luat. (d) Another nematoblastic feature of amphibole is present in the Mae Fah Luang sample under cross-polarized light. Epidote (Ep) aggregates can also be observed.

Amphibole crystals of this group are identified as actinolite (and tremolite?). It exhibits long prismatic subhedral-to-anhedral crystal forms with perfect cleavage. Fibrous aggregates of amphibole are particularly observed in the sample from Na Noi, displaying strong pleochroism of pale yellow-yellowish green-bluish green colors. The observed crystal size ranges from 0.05 to 0.5 mm. No alteration phase of this mineral is present suggesting

near-equilibrium conditions. Thus, this mineral is interpreted to be formed by low-grade regional metamorphisms of mafic parent rocks (Pha Luat, Mae Fah Luang) and results of alteration of clinopyroxene (Na Noi).

Clinopyroxene and plagioclase, on the other hand, are observed in particular samples. Starting with clinopyroxene, it is only observed in the sample from Na Noi exhibiting anhedral and colorless features. The crystals are up to 1 mm in size. The degree of alteration to the amphibole appears as high as 70%. Plagioclase is partially preserved only in the sample from Pha Luat. The crystal size is variable, ranging from 0.1 to 0.8 mm. The crystals are mostly anhedral and formed as porphyroclasts. The alteration of plagioclase to clay minerals and epidote group minerals is distinctly observed throughout the sample. Moreover, the mineral pseudomorphs after plagioclase were commonly found in the Na Noi (30 modal%) and Mae Fah Luang (5.5 modal%) samples. The outlines of platy-to-short prismatic structures having sizes of 0.1–2 mm, along with partial optical properties (e.g., extinction pattern) of plagioclase, are still preserved.

Epidote occurs in subhedral-to-anhedral short-prismatic crystals forming aggregates and/or open-space-filling veinlets (approximately 0.2 mm in width). The crystal size varies from less than 0.1 to 0.5 mm. Weak pleochroic colors of pale pink–pale yellow colorlessness or pale brown colorlessness are observed. No alteration feature of this mineral exists.

Similar to other mafic rocks, opaque iron–titanium oxide minerals are found in all samples. The minerals exhibit irregular anhedral crystals (sizes of 0.05–0.3 mm) with a low degree (10–30%) of alteration to leucoxene. Other minerals, including chlorite, quartz, and carbonate, are associated with the epidote in the veinlets. Chlorite formed in the veinlets exhibits patchy textures of very fine-grained anhedral crystals (less than 0.01 mm in size) with anomalous interference colors of green, greenish-brown, and Berlin blue. However, the chlorite crystals formed in the Na Noi sample (not in the veinlets) show discrete features, including euhedral-to-subhedral tabular forms, fibrous aggregates, and relative coarse-grained sizes (up to 0.1 mm). Anhedral equant quartz grains are 0.01–0.4 mm in diameter and are found in the epidote–chlorite veinlets. Carbonate minerals are present in small anhedral grains (<0.1 mm). They are rarely observed in the epidote–quartz veinlets of the Mae Fah Luang sample.

4.4. Peridotite

The rock samples ($n = 4$) from Phrao are representative of the ultramafic formation in the rock unit DC_v . According to whole-rock composition, the samples are dominated by major abundances of olivine (62–67.25 modal%) associated with minor amounts of clinopyroxene (6.75–9.25 modal%) and plagioclase (9–12.5 modal%). Accessory minerals include chromian spinel and opaque iron–titanium oxides, which are 1.25–2.5 and less than 0.5 modal%, respectively. The secondary-phase minerals are present in various contents ranging from 8.25 to 18 modal% of the whole rock. These minerals are found as serpentine, chlorite, amphibole, biotite, and rarely calcite. Based on the average percentage of primary-phase minerals, these samples have been classified as peridotite.

Under microscopic views, all samples exhibit distinctive cumulus textures comprising cumulus crystals of olivine and chromian spinel, and intercumulus crystals of clinopyroxene, plagioclase, and opaque iron–titanium oxide minerals (Figure 6a,b). The cumulus crystals are perfectly euhedral in shape, whereas the intercumulus crystals are mostly anhedral. Mesh textures of the olivine grains are commonly observed, as well as the pseudomorphs of serpentine/opaque minerals after the olivine (Figure 6c). Pseudomorphs of sericite and clay minerals after plagioclase are also found in all samples. These textures indicate moderate-to-extreme alteration of primary mafic minerals, which were induced by low-grade metamorphism.

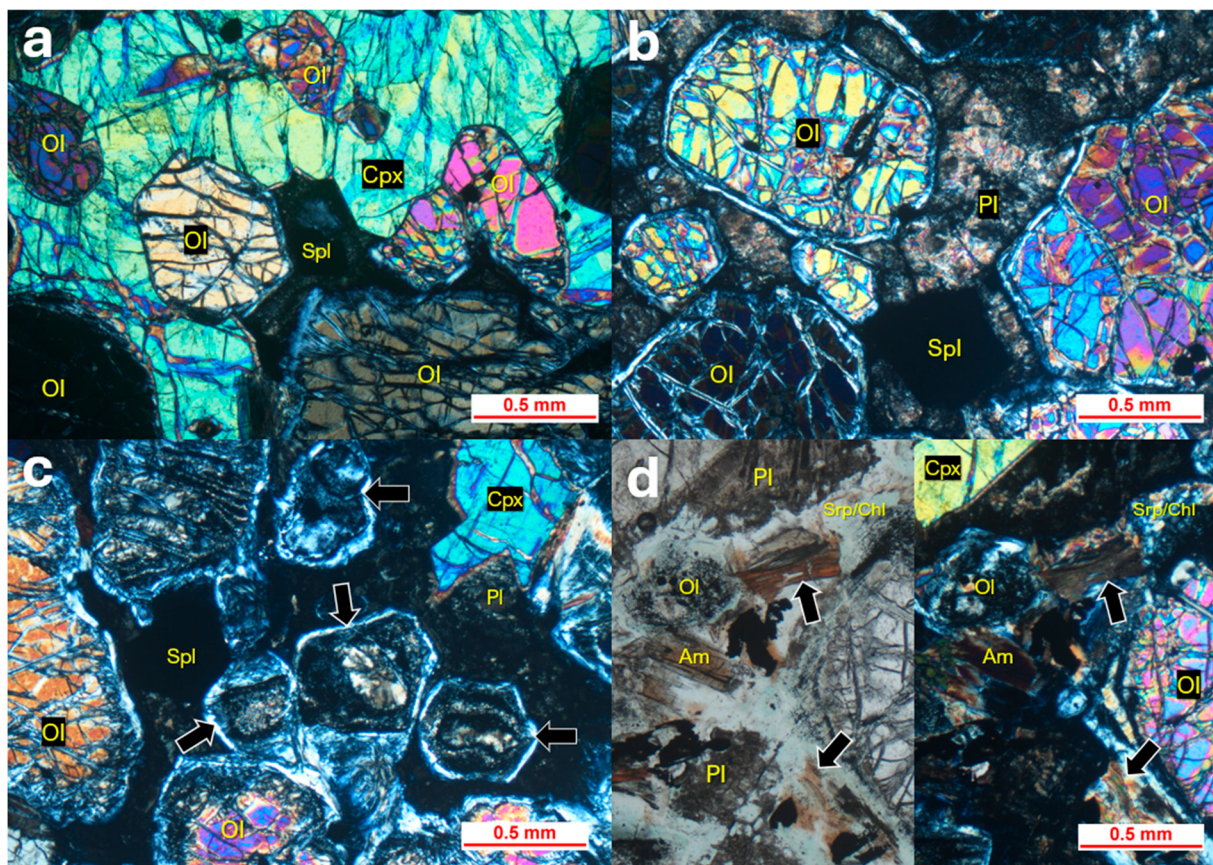


Figure 6. Photomicrographs of peridotite from the rock unit *DCv* showing distinctive cumulus textures: (a) Olivine (Ol) cumulus crystals hosted by intercumulus clinopyroxene (Cpx) present under cross-polarized light. The olivine fractures were filled with serpentine, chlorite, and iron oxide exhibiting mesh texture. Spinel (Spl) is also found as a cumulus crystal. (b) Olivine and spinel cumulus crystals hosted by intercumulus plagioclase (Pl) are observed under cross-polarized light. The plagioclase is currently altered to sericite and clay minerals. Mesh textures are present in olivine. (c) Pseudomorphic serpentine–chlorite–iron oxide mixtures after olivine (arrows) are associated with mesh-textured olivine, euhedral spinel, clinopyroxene, and sericite pseudomorphs after plagioclase observed under cross-polarized light. (d) Secondary amphibole (Am), serpentine/chlorite (Srp/Chl), and biotite (arrows) are associated with the cumulus and intercumulus crystals present under plane- and cross-polarized light. Opaque minerals could indicate iron–titanium oxide minerals.

The olivine crystals observed in the samples are in euhedral forms and exhibit very high relief with highly irregular fractures. The fractures are filled by serpentine associated with chlorite and opaque iron oxides displaying mesh textures under cross-polarized light. The crystal size ranges from 0.1 to 2.5 mm and can be up to 5 mm in some samples. Some olivine crystals contain inclusions of chromian spinel. The overall degree of alteration is moderate (60%).

Besides the olivine, chromian spinel shows translucent-to-opaque euhedral octahedral, dark reddish, brown-colored crystals with a size ranging from 0.1 to 0.7 mm. The mineral also exhibits high relief and isotropic features. Chromite and/or magnetite as the alteration products of the spinel are partially observed along the outer rims.

The intercumulus clinopyroxene, on the other hand, shows anhedral crystal forms with a size of 0.2–1.5 mm. The crystals are pale brown to pale pink in color. The pyroxene grains displaying zoning textures are commonly found in the samples. The alteration of the clinopyroxene to reddish-brown amphibole is also present at a low degree. The developing amphibole cleavages are also observed.

Similar to the pyroxene, the plagioclase observed here is present in the interspaces among the olivine and spinel cumulus crystals. It exhibits anhedral in shape and 0.1–0.8 mm in size. The plagioclase crystals of all samples are completely replaced by fine-grained sericite and clay minerals exhibiting dusty textures. Former prismatic-to-tabular shapes of the plagioclase along with some optical properties (relief, extinction patterns) are well-preserved.

Another intercumulus mineral found in these samples is iron–titanium oxides. These minerals are petrographically assumed as magnetite or ilmenite. They exhibit anhedral forms with a diameter of 0.05–0.2 mm. Their alteration products are found to be leucoxene.

The secondary minerals are certainly found among the cumulus and intercumulus crystals of all samples (Figure 6d). Most of them are near-identical to the alteration products of the primary mineral phases. However, they show slightly discrete optical properties. Pale yellow and pale green colors observed under plane-polarized light indicate secondary-phase serpentine and chlorite mixtures. This phase is different from the pale green serpentine formed in fractured olivine crystals. The secondary amphiboles are locally observed in association with the secondary serpentine and chlorite. It exhibits fibrous aggregates of pale-green-to-green-colored (tremolite) grains. In some cases, reddish-brown platy grains of secondary biotite are also present.

4.5. Altered Pyroxenite

The sample of the rock unit CP_u collected from Huay Lao is classified as an altered product of ultramafic rocks formerly rich in pyroxene. The primary mineral assemblages are predominantly orthopyroxene (60 modal%) and clinopyroxene (28 modal%). Minor amounts of serpentine (8 modal%), talc (2 modal%), chlorite (~1 modal%), and spinel (~1 modal%) are present in crosscutting veinlets or locally disseminated throughout the sample.

Microscopically, the sample shows a cumulus texture comprising coarse-grained high-relief crystals of pyroxenes (Figure 7a,b). Under cross-polarized light, the mesh texture of serpentine (antigorite) is locally observed in some pyroxene grains (Figure 7c). The full replacement by serpentine (chrysotile), talc, uralite, and chlorite is common, indicating an extremely high degree of alteration. The observed textures are crosscut by multiple veinlets of serpentine, talc, and chlorite. The veinlets are 0.1–0.2 mm in width. The outlines and partial optical properties of former pyroxene crystals can be defined.

The pyroxene observed in the sample is entirely altered and replaced by secondary minerals. However, their pseudomorphs are present. Based on shapes and alteration products, the pyroxene can be divided into orthopyroxene-like and clinopyroxene-like features. The orthopyroxene exhibits euhedral-to-subhedral stubby prisms having sizes of up to 1 mm. The parallel extinction and moderate-to-fairly high relief are clearly present. Pseudomorphic serpentine, talc, and uralite after orthopyroxene are also observed. The alteration of orthopyroxene to uralite is distinctly visible under plane-polarized light, exhibiting pale green zones. On the other hand, the clinopyroxene has sizes up to 1.5 mm and exhibits an anhedral-to-subhedral shape, indicating formerly interstitial crystals of the cumulus texture. The clinopyroxene is fully replaced by chlorite, exhibiting colorless under plane-polarized light and Berlin blue interference color under cross-polarized light.

Besides alteration products, serpentine in the form of chrysotile, is present in the veinlets forming fibrous aggregates of very fine-grained crystals (Figure 7d). It exhibits colorless to pale yellow with low relief under plane-polarized light. Its interference colors are gray to yellow, observed in crossed polars. Talc is randomly present and associated with the serpentine veinlets, exhibiting a very fine-grained aggregate. This mineral can be distinguished from serpentine by its higher interference colors (third-order yellow). Moreover, very fine-grained chlorite is locally found in some serpentine veinlets.

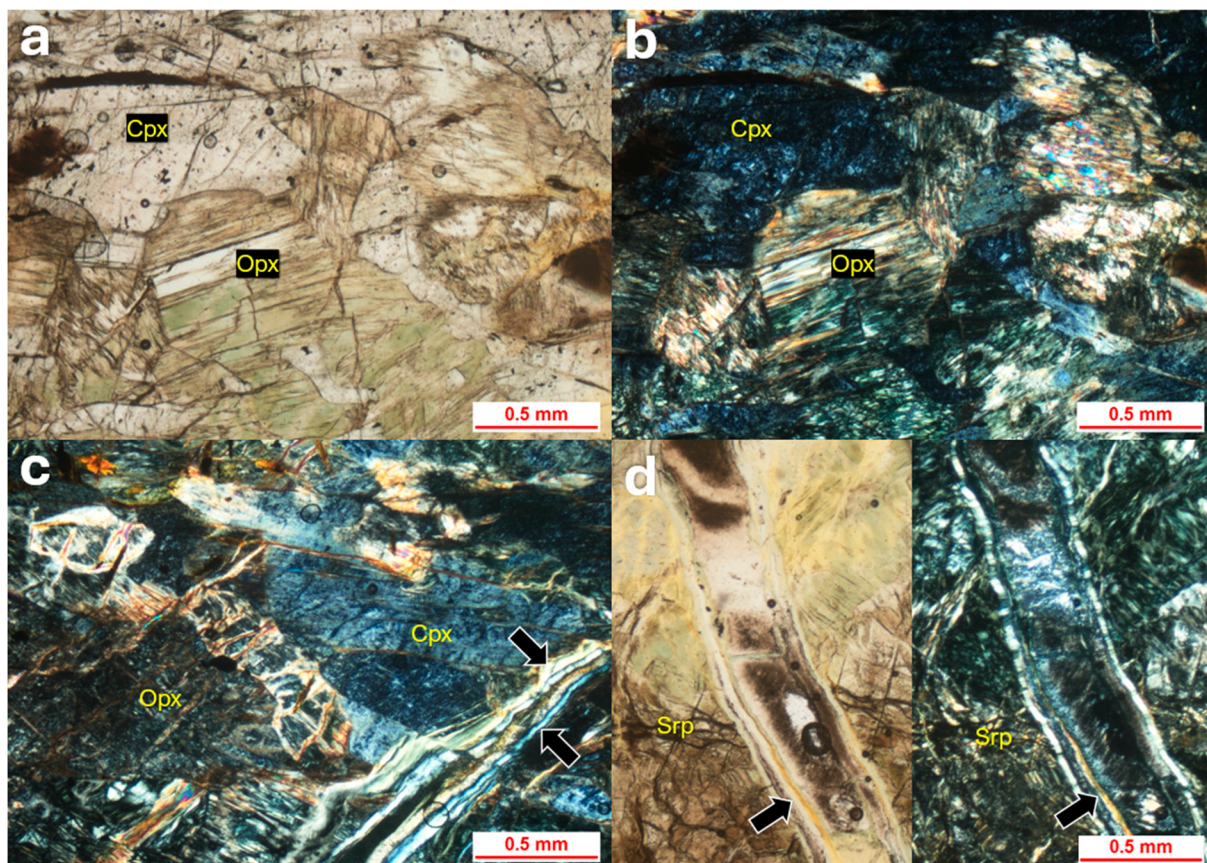


Figure 7. Photomicrographs of altered pyroxenite representing the rock unit CPu collected from Huay Lao showing cumulus textures of former pyroxene-rich ultramafic rocks: (a) Cumulus crystal forms of pale-green orthopyroxene (Opx) and colorless clinopyroxene (Cpx) observed under plane-polarized light. (b) Cross-polarized light image of the same field of view showing that the orthopyroxene altered to serpentine and/or uralite, while the clinopyroxene was fully replaced by chlorite. (c) Mesh textures (antigorite) and fibrous aggregate (chrysotile) occur in the orthopyroxene grains under cross-polarized light. Serpentine–talc veinlets (arrows) crosscut the cumulus pyroxenes. (d) Another serpentine–talc veinlet (arrows) observed under plane- and cross-polarized light. Serpentine (Srp) is also entirely present as fibrous aggregates in the whole rock, indicating a form of chrysotile.

The disseminated crystals of spinel are rarely present in the sample. They are equant euhedral-to-subhedral grains with a size ranging from 0.1 to 0.5 mm. The mineral shows high relief and reddish-brown color (to nearly opaque) under plane-polarized light and isotropic under cross-polarized light. The spinel also contains a moderate degree of alteration (approximately 60%). The alteration products are found to be magnetite and/or chromite occurring along the peripheral rims of the spinel.

4.6. Basaltic Tuff

The last mafic igneous rock provided by this study collected from the Mae On district represents the rock unit PT_{rv} . Based on mineral compositions and volcanic clast sizes, the sample is classified as a coarse lithic tuff or hyaloclastite with mafic composition. Under microscopic views, the sample exhibits pyroclastic texture consisting of multiple-typed fragments in sizes varying from coarse ash (0.06–2.0 mm) to lapilli (>2.0 mm) and surrounding fine-ash matrix (or groundmass?) (<0.06 mm). The overall fragments are 71.68 modal% of the primary composition (or 60.75 modal% of the whole-rock composition), including lithic fragments (58.44% of the fragments), vitric fragments (32.51%), and crystal fragments (9.05%). Approximately 28.32 modal% of the primary composition (or 24.0 modal% of the

whole rock) is identified as a muddy fine-ash brown-colored matrix, possibly indicating the alteration products of volcanic glass precursors. Secondary minerals (15.25 modal% of the whole rock) form as disseminated textures in the entire sample and/or occur as amygdules of the lithic fragments. These minerals include chlorite (8.5 modal%), zeolite (5.0 modal%), palagonite (0.75 modal%), serpentine (0.5 modal%), smectite (0.25 modal%), and opaque minerals (0.25 modal%). Carbonates are also barely observed.

The lithic fragments exhibit basaltic compositions that are divided into three subtypes, including hyalopilitic basalt, crystalline basalt, and vitreous basalt. The most abundant lithic fragments are hyalopilitic basalts found in 46.48 modal% of the lithic fragments (Figure 8a). The fragment sizes range from 0.5 to larger than 2.0 mm. Plagioclase laths and short prismatic clinopyroxene (0.08–0.2 mm) are distinctly present within vitreous groundmass (less than 0.02 mm). Extremely high alteration (70–90%) of plagioclase resulted in sericite and clay mineral formations. Amygdules of chlorite, zeolite, and smectite? are also found in 0.4 mm diameter vesicles. The second most abundant lithic fragment (33.80 modal% of the lithic fragments) is indicated by crystalline basalts. The fragments are relatively large (>2.0 mm in size). They exhibit intergranular-to-subophitic microtextures, consisting of plagioclase (0.02–0.1 mm), clinopyroxene (0.02–0.1 mm), opaque minerals, volcanic glass, and unknown mafic minerals (Figure 8b). The plagioclase is barely altered to the sericite, whereas the volcanic glass and mafic minerals are fully altered to chlorite and clays–opaque minerals, respectively. The glassy or vitreous basalts (scoria?) are observed as 19.72 modal% of the lithic fragments. These fragments are composed of plagioclase and clinopyroxene microphenocrysts and surrounding volcanic glass matrix associated with amounts of vesicles (Figure 8c). Plagioclase microlites are locally found in the matrix. Green-to-pale-brown palagonites, the alteration products of volcanic glass, widely exist throughout the fragments.

The vitric fragments or volcanic glass shards are 0.01–2.0 mm in size, forming vesicle-rich (or scoriaceous), platy, or bubble-walled features. Green-to-brown, clear, and smooth surfaces under plane-polarized light combined with nearly isotropic to weak birefringence in crossed polars reveal the replacement of volcanic glass precursors by the palagonite.

Only two types of crystal fragments are determined in this rock sample, including plagioclase and clinopyroxene (Figure 8d). In general, the crystal shape, size, and alteration degree are slightly identical to those observed in the lithic fragments. The plagioclase (less than 0.5 mm in size) exhibits anhedral shapes with high angularity. The alteration of plagioclase to sericite is extremely high. On the other hand, clinopyroxene crystals are anhedral-to-subhedral and colorless-to-pink with zoning. The crystal sizes are generally up to 0.4 mm. The alteration of clinopyroxene in the thin section is absent.

The minerals and their modal contents observed in all studied samples have thus been summarized as presented in Table 2. The contents of olivine, pyroxene, plagioclase, and serpentine in each sample are involved in the potential CO₂ uptake calculation, as provided in the following discussion.

Supplementary XRD results show detailed possible mineral phases, which could not be obtained by standard petrographic investigation. Mineral assemblages are varied among the samples as shown in Table 3. Plagioclase formed in basalts is identified as labradorite for Den Chai, Sobprab, and Mae Tha samples. Labradorite is also common in other mafic samples. Pyroxene in the form of augite is found in all samples. Actinolite, one of the amphibole-group minerals, is present as a major phase in Mae Chan gabbro-norite and Pha Luat metabasite. This mineral is also observed in basaltic rocks, metabasites, and altered pyroxenite. Olivine, on the other hand, is only observed in basalt and peridotite samples. Even though, the olivine composition shows variable contents of magnesium and iron. The magnesium-rich olivine is more common. Antigorite and chrysotile are

present as serpentine groups. Chrysotile is likely a major phase in the Na Noi metabasite, altered pyroxenite, and basaltic tuff, whereas antigorite is only present in the peridotite. The occurrence of asbestos minerals, including actinolite and chrysotile, in the studied samples is later discussed. Additionally, trace mineral phases in all samples are entirely undetectable due to the equipment limitation.

Table 2. Summary of mineral assemblages and their modal percentage of the studied thin sections obtained from petrographic observation.

Rock Type TS ID [†]	Mineral Assemblage (modal%)																
	Am	Cal	Chl	Ep	Gls	Ol	Opg	Pl	Prh	Px	Qz	Sm	Spl	Srp	Ttn	Zeo	
Basalts <i>DC</i>	—	—	6.00	—	—	10.63	11.00	50.00	—	20.25	—	2.12	—	—	—	—	
	MT	—	—	—	35.90	8.71	—	41.03	—	12.31	—	—	—	2.05	—	—	
	SP	—	—	2.31	—	—	10.63	23.75	38.00	—	14.12	—	11.19	—	—	—	
Gabbronorite <i>MC-1</i>	28.25	—	0.60	—	—	1.00	0.75	29.25	0.58	39.00	—	—	—	—	0.57	—	
	MC-2	3.75	—	3.50	—	—	3.25	11.50	54.75	—	23.25	—	—	—	—	—	
Metabasites <i>PL</i>	45.25	—	3.00	3.25	—	—	3.00	45.25	—	—	0.25	—	—	—	—	—	
	NN	—	—	9.00	17.50	—	—	0.75	30.00	—	42.25	0.50	—	—	—	—	
	MF	67.00	1.00	—	13.50	—	—	3.50	5.50	—	—	9.50	—	—	—	—	
Peridotites <i>PR-1</i>	0.75	—	—	—	—	62.75	—	9.00	—	9.00	—	—	1.25	17.25	—	—	
	PR-2	2.00	0.25	—	—	—	67.00	1.25	12.50	—	6.75	—	—	3.00	7.25	—	—
	PR-3	2.00	—	—	—	—	67.25	0.50	12.50	—	9.25	—	—	1.75	6.75	—	—
	PR-4	3.50	—	—	—	—	62.00	0.25	10.25	—	7.50	—	—	2.50	14.00	—	—
Pyroxenite <i>HL</i>	—	—	15.89	—	—	—	2.52	—	—	—	—	—	2.02	79.57	—	—	
Basaltic tuff <i>MO</i>	—	<0.01	8.50	—	46.13	—	0.25	32.50	—	2.75	—	4.37	—	0.50	—	5.00	

Mineral abbreviation: Am = amphibole, Cal = calcite, Chl = chlorite, Ep = epidote, Gls = volcanic glass, Ol = olivine, Opg = opaque minerals (Fe-Ti oxides), Pl = plagioclase, Prh = prehnite, Px = pyroxene, Qz = quartz, Sm = smectite, Spl = spinel, Srp = serpentine/talc, Ttn = titanite, Zeo = zeolite. [†] Thin section ID: MT = Mae Tha, SP = Sobrab, DC = Den Chai, MC = Mae Chan, PL = Pha Luat, MF = Mae Fah Luang, NN = Na Noi, PR = Phrao, HL = Huay Lao, MO = Mae On.

Table 3. Semiquantitative results of the rock samples obtained from X-ray diffraction technique.

Rock Type: ID [†]	Unit	Mineral Phase *			
		Major [>30%]	Moderate [10–30%]	Minor [2–10%]	Trace [<2%]
Olivine basalt: MT	bs	Lab	Act, Aug	n/d	n/d
Olivine basalt: SP	bs	Ol	Lab, Aug	Sa	n/d
Olivine basalt: DC	bs	Lab	Aug, Chl, Ctl	Act	n/d
Gabbronorite: MC	CP _u	Act	Lab, Chl, Sa	Aug, Qz, Cal	n/d
Metabasite: PL	C _b	Act	Lab, Mc, Ctl	Py, Aug, Chl	n/d
Metabasite: MF	CP _u	Lab	Aug, Ctl, Act	Chl	n/d
Metabasite: NN	CP _u	Ctl	Act, Lab	Chl, Aug	n/d

Table 3. Cont.

Rock Type: ID [†]	Unit	Mineral Phase *			
		Major [>30%]	Moderate [10–30%]	Minor [2–10%]	Trace [<2%]
Peridotite: PR	DC _v	-	Atg, Aug, Ol, Ab, Chl	Ill, Cal	n/d
Altered pyroxenite: HL	CP _u	Ctl, Aug	Act	Chl	n/d
Basaltic tuff: MO	PT _{rv}	Ctl	Cal, Chl	Lab, Act, Aug	n/d

n/d = undetectable. * Mineral abbreviation: Ab = albite, Act = actinolite, An = anorthite, Ano = anorthosite, Atg = antigorite, Aug = augite, Cal = calcite, Chl = chlorite, Ctl = chrysotile, Hem = hematite, Ill = illite, Lab = labradorite, Mag = magnetite, Mc = microcline, Mnt = montmorillonite, Ol = olivine, Py = pyrite, Qz = quartz, Sa = sanidine. [†] ID abbreviation: MT = Mae Tha, SP = Sobprab, DC = Den Chai, MC = Mae Chan, PL = Pha Luat, MF = Mae Fah Luang, NN = Na Noi, PR = Phrao, HL = Huay Lao, MO = Mae On.

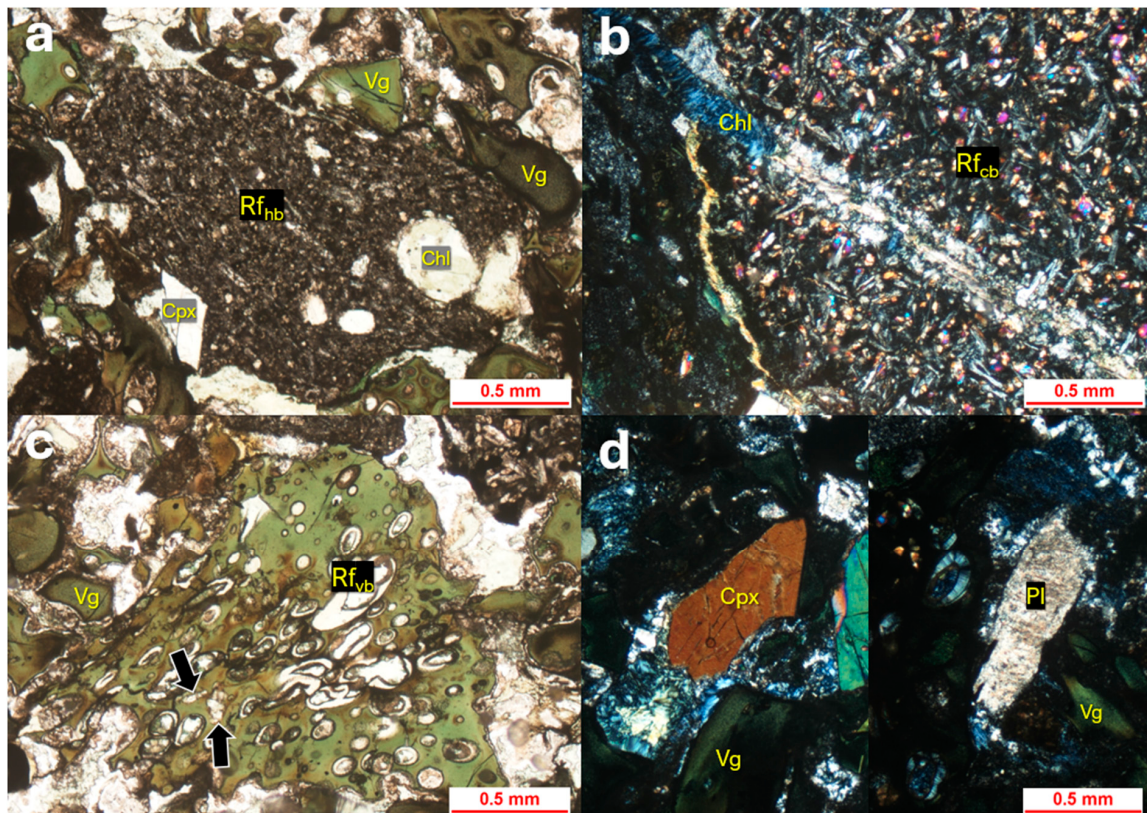


Figure 8. Photomicrographs of basaltic tuff from the rock unit *PT_{rv}* showing mafic lithic components associated with multiple fragments of volcanic glass and crystals: (a) Hyalopilitic basaltic fragment (*Rf_{hb}*) comprising coarse-grained clinopyroxene (Cpx), fine-grained plagioclase and vitreous groundmass, and amygdules of chlorite (Chl) observed under plane-polarized light. Volcanic glass fragments (Vg) exhibiting pale green-to-brown colors of palagonite are also present. (b) Large-sized crystalline basaltic fragment (*Rf_{cb}*) crosscutting by secondary chloritic veinlet observed under cross-polarized light. (c) Vitreous basaltic fragment (*Rf_{vb}*) showing a pale green-to-brown vesicular texture observed under plane-polarized light. Clinopyroxene microphenocrysts are indicated by arrows. The vesicles are filled with chlorite. (d) Cross-polarized light images of two fields of view showing individual clinopyroxene and plagioclase fragments associated with vitric fragments. The alteration of clinopyroxene is low, whereas the plagioclase is highly altered to sericite.

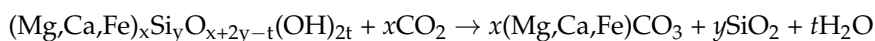
5. Discussion

5.1. CO₂-Reactive Minerals in Mafic and Ultramafic Rocks

It is known that mafic and ultramafic igneous rocks are major sources of magnesium-, calcium-, and/or iron-rich silicate minerals, playing a crucial role in carbon sequestration

through CO₂–rock interactions, with or without the presence of water [9,25,29,60,70]. These minerals, including plagioclase, olivine, pyroxene, and serpentine, have relatively high reactivity with CO₂ compared with other silicates [21,31,52,71,72]. The high abundance of CO₂-reactive silicates observed in most studied samples, especially peridotite, pyroxenite, gabbro, and basalt, apparently provides potential for mineral CO₂ sequestration. The basaltic tuff and some metabasites, on the other hand, contain only minor amounts of reactive minerals that could result in opposite directions.

CO₂ mineralization reactions are naturally spontaneous and exothermic. The mineral reaction rate also depends on initial mineral species and surrounding conditions. The reaction starts when the CO₂-reactive mineral interacts with the CO₂-dissolved solution. The acidic aqueous condition induces the mineral breakdowns, releasing divalent cations (Mg²⁺, Ca²⁺, Fe²⁺) into the solution. These cations subsequently pair with molecules of bicarbonate in the solution, resulting in a carbonate mineral precipitation [39,73–75]. Complex elemental compounds of the reactive minerals yield compositional variations in carbonate species products. Silica in solid or aqueous forms is also a common byproduct of the reactions. The general form of CO₂ mineralization reaction is as follows [19,57,76]:



According to mineral reactions, several previous studies have proposed the theoretical estimation of the maximum potential CO₂ uptake for each reactive mineral, presenting on a percentage weight by weight, as shown in Table 4 [12,21,25,71,72,77–79]. The CO₂ uptake potential varies among mineral groups and their end members.

Table 4. Theoretical CO₂ uptake potential of reactive minerals, assuming completion of CO₂ mineralization [12,21,25,71,72,77–79].

Mineral Group	End Member	Chemical Formula	Atomic Weight (g/mol)	* Reactive CO ₂ (mol)	Calculated CO ₂ Uptake (%wt/wt)
Olivine	Forsterite	Mg ₂ SiO ₄	140.691	2	62.56
	Fayalite	Fe ₂ SiO ₄	203.771	2	43.19
Pyroxene	Augite	(Ca,Na)(Mg,Fe,Al,Ti)Si ₂ O ₆	222.448	2	39.57
	Diopside	CaMgSi ₂ O ₆	216.547	2	40.65
	Enstatite	MgSiO ₃	100.387	1	43.84
	Hypersthene	(Mg,Fe)SiO ₃	116.157	1	37.89
	Ferrosilite	FeSiO ₃	131.927	1	33.36
	Wollastonite	CaSiO ₃	116.160	1	37.89
Plagioclase	Albite	NaAlSi ₃ O ₈	262.220	1	16.78
	Labradorite	(Ca,Na)(Al,Si) ₄ O ₈	269.659	1	16.32
	Anorthite	CaAl ₂ Si ₂ O ₈	278.203	1	15.82
Serpentine	Antigorite	Mg ₃ (Si ₂ O ₅)(OH) ₄	277.108	3	47.64
	Chrysotile	Mg ₃ (Si ₂ O ₅)(OH) ₄	277.108	3	47.64
	Lizardite	Mg ₃ (Si ₂ O ₅)(OH) ₄	277.108	3	47.64

* Atomic weight of CO₂ = 44.009 g/mol.

Olivine is believed to be the most reactive silicate with CO₂. It naturally represents a solid-solution series between magnesium-rich (forsterite) and iron-rich (fayalite) end members. Ionic substitution of Mg²⁺ and Fe²⁺ for each other in olivine results in different CO₂ uptake estimations. Nearly 1.6 tons of forsterite are required to sequester a ton of CO₂, whereas approximately 2.3 tons of fayalite are required to bind the same amount of CO₂ [57,77,80]. The most naturally occurring olivines in mafic and ultramafic igneous rocks are forsterite, whereas fayalite is more abundant in felsic and intermediate rocks [81]. Regarding the rock types and XRD data, most olivines observed in the studied samples

are convincing magnesium-rich end members. The olivine contents are unsurprisingly varied among different formations, ranging from 0 to 67.25 modal%. The highest content is found in the peridotite, whereas the metabasites, altered pyroxenite, and mafic tuff are olivine-free. The moderate and low olivine contents are observed in the basalts and gabbronorites, respectively. The rocks containing higher olivine contents tend to provide higher CO₂ uptake percentages.

Pyroxene can be divided into orthopyroxene and clinopyroxene subgroups based on crystal structures and optical properties. There are a number of pyroxene end members that occur in various geologic settings. The most common orthopyroxene and clinopyroxene members formed in igneous rocks are magnesium-rich (enstatite) and magnesium- and calcium-rich (augite), respectively [82]. According to the CO₂ uptake potential, enstatite sequesters slightly larger amounts of CO₂ than augite. Sequestering a ton of CO₂ needs a 2.3-ton enstatite, whereas a 2.5-ton augite is required for a ton of CO₂ sequestration [25,79]. Several studies have previously reported the fastest reaction rate of wollastonite, a calcium-rich clinopyroxene [8,83–85]. However, it occasionally forms during metasomatisms of calcium-rich formations by silica-bearing fluids, sometimes resulting in skarns. Limited resource availability and various industrial applications of wollastonite may be unworthy of mineral CO₂ sequestration technology [86]. The pyroxenes observed in the mafic and ultramafic samples distinctly comprise enstatite and augite, ranging from 0 to 88 modal%. The altered pyroxenite sample shows the highest contents of pyroxene, whereas moderate pyroxene contents are found in basalts, gabbronorites, and Na Noi metabasite. Basaltic tuff and other metabasites are lacking in pyroxene.

Similarly to the olivine series, plagioclase forms a solid solution series between sodium-rich (albite) and calcium-rich (anorthite) end members. Variations in calcium-sodium contents can divide the plagioclase series into six members. The most common member in mafic igneous rocks is labradorite, the calcium, sodium-rich species. The percentage of potential CO₂ uptake by labradorite is certainly in the middle range between albite and anorthite. Approximately 6.1-ton labradorite is required for blinding a ton of CO₂. Compared with olivine and pyroxene, the plagioclase clearly shows lesser uptake potential as it demands a larger amount of the mineral to blind a ton of CO₂. Moreover, the dissolution rate of plagioclases is relatively slow, resulting in low reactivity with CO₂ [74,87]. The plagioclases observed in this study are entirely labradorite based on their optical properties and XRD data. The mineral content ranges from 0 to 54.75 modal%. The mafic rocks, including basalts, gabbronorites, metabasites, and tuff, show high contents of plagioclase, meanwhile, the peridotites show moderate contents. Only altered pyroxenite is lacking in plagioclase.

Another promising CO₂-reactive mineral focused on in this study is a serpentine group. Even though it is not a primary mineral formed in igneous rocks, it is particularly found in large deposits worldwide [27]. Serpentine has been known as a magnesium-rich hydrous silicate formed by the metamorphism or alteration of mafic minerals. Several serpentine polymorphs, including antigorite, chrysotile, and lizardite, share an identical potential CO₂ uptake percentage of 47.64 percent. However, the substitution of Fe²⁺ for Mg²⁺ certainly occurs in the serpentine-group minerals, resulting in a drop in its CO₂ uptake potential. The mass ratio of serpentines to CO₂ required for carbon sequestration ranges from 2.10 to 2.51 [25,77,80,86]. The serpentine members found in this study are predominantly antigorite and chrysotile based on crystal habits, optical properties, and XRD data. The antigorite member is commonly observed in the peridotites, exhibiting 6.75–17.25 modal%. It is also found in the basaltic tuff with less than 1 modal%. Minor amounts of chrysotile, on the other hand, are locally found in the altered pyroxenite.

In addition, several other silicate minerals are observed in some studied samples, especially in metabasites and pyroxene–hornblende gabbronorite. The minerals include hornblende, actinolite, tremolite, chlorite, and/or epidote. Spinel, chromian spinel, chromite, and magnetite are minorly observed in the peridotites, whereas ilmenite and magnetite are present in the mafic rocks. The existence of these minerals in the rocks affects the overall efficiency evaluation of the mineral CO₂ sequestration. However, these minerals are mostly thermodynamically stable at the surface or near-surface environments and their chemical reactions with CO₂ are quite complex. These minerals thus have been excluded from the CO₂ uptake estimations of this study.

5.2. Primary Assessment of Potential CO₂ Uptake

The CO₂ uptake ability of rocks is certainly influenced and controlled by their mineral assemblage [25,61,86,87]. For example, dunite, an ultramafic rock comprising more than 90% olivine, tends to have a CO₂ uptake potential nearly equal to that of olivine (<62.56%). On the other hand, the average CO₂ uptake of serpentinite, a serpentine-rich metamorphic rock, is almost identical to that of serpentine (<47.64%) [86]. The studied mafic and ultramafic rocks show variable contents of reactive minerals, including olivine, pyroxene, plagioclase, and serpentine. These subsequently affect the potential CO₂ uptake prediction of each rock type. For instance, this study assumes that more than 60 modal% olivine of the peridotites significantly yields a mass ratio of the rocks to CO₂ required for carbon sequestration. The CO₂ uptake ability of the remaining minerals (serpentine, plagioclase, pyroxene) is also considered to partially contribute to the whole rocks, relating to the mineral contents. This conceptual idea is then applied to other rock types. The total CO₂ uptake of each rock is then calculated from a sum of products between reactive mineral content and its potential CO₂ uptake percentage, as shown in Table 5. The CO₂ uptake potential calculation provided by this work is specifically based on the petrographic modal analytical results, since the XRD data of this study are only used to indicate mineral phases. Furthermore, advanced microanalytical techniques are strongly recommended to investigate the target rocks quantitatively and qualitatively for the next advanced exploration stages.

Mineralogical variations in the rocks particularly result in different percentages of the estimated CO₂ uptake. Several previous studies have been reported on the mass ratios of rock to CO₂ required for mineral CO₂ sequestration, including dunite (1.8) [86], serpentinite (2.3) [86], talc (2.6) [88], wehrlite (1.9–2.4) [61], and basalt (5–7.1) [12,78,86]. Unsurprisingly, the studied ultramafic rocks, i.e., peridotites and altered pyroxenite, show relatively high percentages of potential CO₂ uptake compared with the mafic rocks. According to Table 4, the calculated mass ratio of peridotite to CO₂ required for CO₂ uptake is estimated to be 1.9–2, while that of altered pyroxenite is around 2.4. The mass ratios of basalt or gabbronorite to CO₂ for CO₂ uptake apparently range from 4.4 to 6. Metabasite samples, however, show a wide range of CO₂ uptake percentages. The Na Noi metabasite has the highest percentage, which is nearly equal to those of basalts and gabbronorites. Meanwhile, the CO₂ uptake percentage of Pha Luat metabasite is yielded by its plagioclase content. Lacking reactive target minerals of Mae Fah Luang metabasite thus results in a very low CO₂ uptake percentage. The carbon sequestration potential of metamorphic rocks presumably depends on protolith type, metamorphic process, and degree of metamorphism. On the other hand, the basaltic tuff has an unexpectedly low CO₂ uptake percentage. Based on its reactive mineral contents, the mass ratio of rock to CO₂ required for CO₂ uptake is estimated to be as high as 15.1 compared with mafic rocks. The complex volcanic components associated with undefined phases in the rock could make it hard to precisely determine the CO₂-reactive mineral composition and thus the uptake potential.

Table 5. Estimating potential CO₂ uptake of the studied rock samples based on their reactive mafic mineral contents obtained by petrographic modal analysis.

Rock Type	Olivine		Pyroxene		Plagioclase		Serpentine		Total CO ₂ Uptake
	Modal%	%CO ₂ Uptake	Modal%	%CO ₂ Uptake	Modal%	%CO ₂ Uptake	Modal%	%CO ₂ Uptake	
Olivine basalts	10.63	6.65	20.25 ^a	8.01	50.00	8.16	—	—	22.82% ¹
	8.71	5.45	12.31 ^a	4.87	41.03	6.49	—	—	16.81% ²
	10.63	6.65	14.13 ^a	5.59	38.00	6.20	—	—	18.44% ³
Gabbronorite	3.25	2.03	17.25 ^a 6.00 ^b	6.83 2.63	54.75	8.94	—	—	20.43%
Px-Hbl gabbronorite	1.00	0.63	21.25 ^a 17.75 ^b	8.41 7.78	29.25	4.77	—	—	21.59%
Metabasite	—	—	—	—	45.25	7.38	—	—	7.38% ⁴
	—	—	—	—	5.50	0.90	—	—	0.90% ⁵
	—	—	42.25 ^a	16.72	30.00	4.90	—	—	21.62% ⁶
Peridotite	62.75	39.26	9.00 ^a	3.56	9.00	1.47	17.25 ^d	8.22	52.51%
	67.00	41.92	6.75 ^a	2.67	12.50	2.04	7.25 ^d	3.45	50.08%
	67.25	42.07	9.25 ^a	3.66	12.50	2.04	6.75 ^d	3.22	50.99%
	62.00	38.79	7.50 ^a	2.97	10.25	1.67	14.00 ^d	6.67	50.10%
Altered pyroxenite	—	—	28.00 ^a 60.00 ^b	11.08 26.30	—	—	8.00 ^e	3.81	41.19%
Basaltic tuff	—	—	2.75 ^a	1.09	32.50	5.30	0.5 ^d	0.24	6.63%

^a clinopyroxene (augite), ^b orthopyroxene (enstatite), ^c antigorite, ^d chrysotile, ¹ Den Chai, ² Mae Tha, ³ Sobprab, ⁴ Pha Luat, ⁵ Mae Fah Luang, ⁶ Na Noi.

The CO₂ mineralization of rocks is potentially controlled by the dissolution of olivine since the mineral has a high reactivity with CO₂ [44,89]. Regarding Table 5, this study strongly supports that olivine-rich rocks should be considered the best targets for Carbon Geological Sequestration by CO₂ mineralization. The second-best targets for mineral CO₂ sequestration could be considered for pyroxene-rich rocks. However, the abundance or availability of resources and exploration-to-production costs must be accounted for proper target selections. Furthermore, the alterations of the rocks or minerals highly affect their overall CO₂ uptake potential [61]. The partial-to-full alteration of olivine to iddingsite (in basalts) or serpentine (in peridotites) observed in this study appears to reduce the potential CO₂ uptake percentage. Hence, this study agrees that the existing CO₂-reactive minerals and their modal contents could be used as one of the first evidence for predicting the carbon sequestration potential of each geological formation. The potential CO₂ uptake calculation provided here might also be applied to other relevant rock formations. Further, advanced microanalyses and laboratory experiments of these rock types with CO₂ are strongly recommended to provide an understanding of rock–CO₂ interactions on a lab scale.

5.3. Implications for Enhanced Rock Weathering Technology

Rocks with mafic and ultramafic compositions have been widely recognized as targets for CO₂ sequestration via enhanced rock weathering techniques. Many earlier ERW studies have estimated the CO₂ removal rates of natural basalts, pure mafic silicates (i.e., olivine, wollastonite, and serpentine), and ultramafic mine wastes through various study types, including experiments, field trials, and modeling [8,44,45,90–94]. They have reported a wide range of CO₂ removal rates, which were subsequently discussed to be influenced

by rock types, analytical quantification approaches, area climate, and environmental conditions. The studied mafic rock types, especially basalts, could be linked to a number of various-scale ERW projects for CO₂ sequestration by applying crushed basaltic rocks in natural tropical ecosystem settings, agricultural fields, and/or urban areas, in Asia, Brazil, the UK, and the USA [50,51,94–99]. It is initially proposed that the basalts and gabbros, as well as peridotites and altered pyroxenite, could be convincing targets for ERW in Thailand.

However, it is necessary to take into account that olivine and chromite, which are abundant in ultramafic rocks, potentially release harmful toxic elements (i.e., nickel and chromium) and associated asbestos minerals into the environments despite rapid reactivity with CO₂ [45,50,95]. Regarding petrographic observation, the studied samples containing significant amounts of fibrous amphibole and fibrous serpentine, include metabasites, altered pyroxenite, and peridotites. The supported XRD data indicates that those minerals are mostly actinolite and chrysotile, which are both toxic asbestoses. Even though the most serpentine minerals in the peridotites are antigorite, the high content of olivine and the existing chromite in these rocks potentially increase environmental and health concerns. These could unsurprisingly remove the altered pyroxenite, peridotites, and metabasites from the best candidate list for ERW. On the other hand, the basalts, especially the Sobrab sample, seem to be the best candidates due to their relatively low asbestos mineral contents compared with others. Besides, the gabbronorites appear to be the second choice, as they are free of fibrous amphiboles and serpentines observed under the microscope. However, their XRD data shows a major content of actinolite. Understanding the mineral assemblage and textural characteristics of target rocks is important to selecting the best geological candidate and engineering design for ERW.

Besides suitable rock types, the north region of Thailand is certainly characterized by a subtropical savanna climate. Hot-to-warm and humid conditions sufficiently promote the physical and chemical weathering process of the rocks [50,51]. Furthermore, conducting lab-to-field-scale experiments and/or geochemical modeling of these rocks under real-world chemical weathering conditions is highly recommended.

Since the CO₂-rock interaction rate is proportional to the reactive surface area of the rock, increasing the rock's surface area practically improves the rate of enhanced rock weathering. The surface area typically increases with a decrease in rock particle size during the rock crushing and grinding process [100,101]. The grain sizes of crushed rocks used in ERW commonly range from microns to millimeters. The finest-sized rocks commonly show a relatively fast weathering rate [100,102]. However, the processes of crushing and grinding ERW rocks to very fine particle sizes are energy- and time-consuming.

Determining the mineral size range of target rocks has been believed to be crucial in optimal size selection for ERW applications [61,91,103]. The ultramafic rocks of this study exhibit coarse-grained textures and have average grain sizes of 0.05–5 mm (peridotites) and 0.1–1.5 mm (altered pyroxenite). The mafic rocks, on the other hand, can be separated into intrusive (gabbronorites) and extrusive (basalts, basaltic tuff) origins. The grain sizes of the intrusive rocks range from 0.05 to 5 mm (as of gabbronorites), which are undoubtedly coarser than those of the extrusive rocks (0.01–2 mm). Similar to the basalt, the metabasites show average grain sizes of 0.01–2 mm. Nonetheless, it seems to be practical to consider the average and/or smallest size of the most CO₂-reactive minerals, especially olivine, formed in that particular rock to be a target size for ERW. For example, the average size of olivine in the peridotite and basalt are 0.1 and 0.05 mm, respectively. Reducing the rock size to match its olivine size should effectively increase its reactive surface areas. Additionally, byproducts from mafic and ultramafic rock quarries (rock dust and rock flour) or mines (tailings) can be further considered as alternative options since they already have relatively high surface areas. Besides, using these waste-like materials potentially reduces production

costs and provides sustainable uses of the materials for carbon sequestration. However, it is necessary to determine the material chemical compositions and evaluate their CO₂ mineralization potential, as well as mineral toxicity, before applying them directly to the environment. Furthermore, experimental studies testing the physical and mechanical behaviors of these rocks and relevant materials are strongly recommended to preliminarily design specific rock milling plants, providing raw material supplies for mineral CO₂ sequestration and ERW industries.

6. Conclusions

The petrographic investigation conducted here has fully reported the mineralogy and textural characteristics of mafic and ultramafic rocks exposed in northern Thailand. Their modal mineralogy, textures, and associated features, such as alteration and/or deformation, provide a primary assessment of potential CO₂ uptake for carbon sequestration by CO₂ mineralization. This study agrees that the contents of CO₂-reactive minerals, especially olivine, pyroxene, plagioclase, and serpentine, appear to control the potential CO₂ uptake of rocks. The ultramafic rocks, including peridotites and altered pyroxenite, have higher CO₂ uptake percentages than those of gabbros and basalts. The CO₂ uptake potential of basaltic tuff is low despite its mafic-related name. Metabasites, on the other hand, show a wide range of CO₂ uptake potential due to compositional variations and the absence of reactive minerals. However, it is also believed that the alteration of reactive minerals in the rock sufficiently results in an overestimate of its CO₂ uptake potential. Besides, the rocks containing significant contents of toxic elements or asbestos minerals, might not be suitable candidates for ERW. Reducing the initial rock size to the average or smallest size of the CO₂-reactive minerals observed under a microscope may provide sufficient reactive surface areas for mineral CO₂ sequestration. Determining the CO₂-reactive mineral size ranges of each target rock could be applied to an engineering design for ERW applications. Since the natural rocks are mineralogical and textural variables among rock types and geological settings, understanding their mineralogical–textural characteristics and estimated CO₂ uptake potential could be an earlier step in the georesource exploration for CO₂ drawdown through ERW technology and mitigating climate change.

Supplementary Materials: The following supporting information can be downloaded at: <https://www.mdpi.com/article/10.3390/geosciences15030089/s1>, PowDLL-XRD.xlsx containing converted raw data of all studied samples; individual ten PNG files of XRD diffractograms.

Funding: This research is funded by the National Research Council of Thailand (NRCT), grant number N42A660939.

Data Availability Statement: The original contributions presented in this study are included in the article and the Supplementary Materials. Further inquiries can be directed to the author.

Acknowledgments: The author thanks Khomchan Promneewat from the South Dakota School of Mines and Technology for his advice on the digital geologic map of Thailand. The author also thanks the Department of Mining and Petroleum Engineering, Chiang Mai University, for providing all facilities used in this work.

Conflicts of Interest: The author declares no conflicts of interest.

References

1. Bachu, S. Sequestration of CO₂ in geological media: Criteria and approach for site selection in response to climate change. *Energy Convers. Manag.* **2000**, *41*, 953–970. [[CrossRef](#)]
2. Holloway, S. Carbon dioxide capture and geological storage. *Philos. Trans. A Math. Phys. Eng. Sci.* **2007**, *365*, 1095–1107. [[CrossRef](#)]
3. Bachu, S. CO₂ storage in geological media: Role, means, status and barriers to deployment. *Prog. Energy Combust. Sci.* **2008**, *34*, 254–273. [[CrossRef](#)]

4. Larachi, F.; Daldoul, I.; Beaudoin, G. Fixation of CO₂ by chrysotile in low-pressure dry and moist carbonation: Ex-situ and in-situ characterizations. *Geochim. Cosmochim. Acta* **2010**, *74*, 3051–3075. [[CrossRef](#)]
5. Michael, K.; Golab, A.; Shulakova, V.; Ennis-King, J.; Allinson, G.; Sharma, S.; Aiken, T. Geological storage of CO₂ in saline aquifers—A review of the experience from existing storage operations. *Int. J. Greenh. Gas Con.* **2010**, *4*, 659–667. [[CrossRef](#)]
6. Santos, R.; Van Audenaerde, A.; Chiang, Y.; Iacobescu, R.; Knops, P.; Van Gerven, T. Nickel extraction from olivine: Effect of carbonation pre-treatment. *Metals* **2015**, *5*, 1620–1644. [[CrossRef](#)]
7. Ciais, P.; Sabine, C.; Bala, G.; Bopp, L.; Brovkin, V.; Canadell, J.; Chhabra, A.; Defries, R.; Galloway, J.; Heimann, M. *Climate Change 2013: The Physical Science Basis*; Cambridge University Press: Cambridge, UK, 2013.
8. National Academies of Sciences, Engineering, and Medicine; Division on Earth and Life Studies; Ocean Studies Board; Board on Chemical Sciences and Technology; Board on Earth Sciences and Resources; Board on Agriculture and Natural Resources; Board on Energy and Environmental Systems; Board on Atmospheric Sciences and Climate; Committee on Developing a Research Agenda for Carbon Dioxide Removal and Reliable Sequestration. *Negative Emissions Technologies and Reliable Sequestration: A Research Agenda*; The National Academies Press: Washington, DC, USA, 2019.
9. Kelemen, P.; Benson, S.M.; Pilorgé, H.; Psarras, P.; Wilcox, J. An overview of the status and challenges of CO₂ storage in minerals and geological formations. *Front. Clim.* **2019**, *1*, 9. [[CrossRef](#)]
10. Raza, A.; Glatz, G.; Gholami, R.; Mahmoud, M.; Alafnan, S. Carbon mineralization and geological storage of CO₂ in basalt: Mechanisms and technical challenges. *Earth-Sci. Rev.* **2022**, *229*, 104036. [[CrossRef](#)]
11. Béarat, H.; McKelvy, M.J.; Chizmeshya, A.V.; Gormley, D.; Nunez, R.; Carpenter, R.W.; Squires, K.; Wolf, G.H. Carbon sequestration via aqueous olivine mineral carbonation: Role of passivating layer formation. *Environ. Sci. Technol.* **2006**, *40*, 4802–4808. [[CrossRef](#)]
12. Sanna, A.; Uibu, M.; Caramanna, G.; Kuusik, R.; Maroto-Valer, M.M. A review of mineral carbonation technologies to sequester CO₂. *Chem. Soc. Rev.* **2014**, *43*, 8049–8080. [[CrossRef](#)]
13. Mwenketishi, G.; Benkreira, H.; Rahamanian, N. Carbon dioxide sequestration methodologies—A review. *Am. J. Clim. Change* **2023**, *12*, 579–627. [[CrossRef](#)]
14. Kelemen, P.B.; Matter, J.; Streit, E.E.; Rudge, J.F.; Curry, W.B.; Blusztajn, J. Rates and mechanisms of mineral carbonation in peridotite: Natural processes and recipes for enhanced, in situ CO₂ capture and storage. *Annu. Rev. Earth Planet. Sci.* **2011**, *39*, 545–576. [[CrossRef](#)]
15. Wilson, S.A.; Harrison, A.L.; Dipple, G.M.; Power, I.M.; Barker, S.L.L.; Ulrich Mayer, K.; Fallon, S.J.; Raudsepp, M.; Southam, G. Offsetting of CO₂ emissions by air capture in mine tailings at the Mount Keith Nickel Mine, Western Australia: Rates, controls and prospects for carbon neutral mining. *Int. J. Greenh. Gas Con.* **2014**, *25*, 121–140. [[CrossRef](#)]
16. Sigfusson, B.; Gislason, S.R.; Matter, J.M.; Stute, M.; Gunnlaugsson, E.; Gunnarsson, I.; Aradottir, E.S.; Sigurdardottir, H.; Mesfin, K.; Alfredsson, H.A.; et al. Solving the carbon-dioxide buoyancy challenge: The design and field testing of a dissolved CO₂ injection system. *Int. J. Greenh. Gas Con.* **2015**, *37*, 213–219. [[CrossRef](#)]
17. Hariharan, S.; Mazzotti, M. Kinetics of flue gas CO₂ mineralization processes using partially dehydroxylated lizardite. *Chem. Eng. J.* **2017**, *324*, 397–413. [[CrossRef](#)]
18. Liu, R.; Heinemann, N.; Liu, J.; Zhu, W.; Wilkinson, M.; Xie, Y.; Wang, Z.; Wen, T.; Hao, F.; Haszeldine, R.S. CO₂ sequestration by mineral trapping in natural analogues in the Yinggehai Basin, South China Sea. *Mar. Pet. Geol.* **2019**, *104*, 190–199. [[CrossRef](#)]
19. Lackner, K.S.; Wendt, C.H.; Butt, D.P.; Joyce, E.L.; Sharp, D.H. Carbon dioxide disposal in carbonate minerals. *Energy* **1995**, *20*, 1153–1170. [[CrossRef](#)]
20. Kelemen, P.B.; Matter, J. In situ carbonation of peridotite for CO₂ storage. *Proc. Natl. Acad. Sci. USA* **2008**, *105*, 17295–17300. [[CrossRef](#)]
21. Oelkers, E.H.; Gislason, S.R.; Matter, J. Mineral carbonation of CO₂. *Elements* **2008**, *4*, 333–337. [[CrossRef](#)]
22. Power, I.M.; Wilson, S.A.; Dipple, G.M. Serpentinite Carbonation for CO₂ Sequestration. *Elements* **2013**, *9*, 115–121. [[CrossRef](#)]
23. Matter, J.M.; Stute, M.; Snaebjornsdottir, S.O.; Oelkers, E.H.; Gislason, S.R.; Aradottir, E.S.; Sigfusson, B.; Gunnarsson, I.; Sigurdardottir, H.; Gunnlaugsson, E.; et al. Rapid carbon mineralization for permanent disposal of anthropogenic carbon dioxide emissions. *Science* **2016**, *352*, 1312–1314. [[CrossRef](#)] [[PubMed](#)]
24. Gunnarsson, I.; Aradóttir, E.S.; Oelkers, E.H.; Clark, D.E.; Arnarson, M.P.; Sigfusson, B.; Snæbjörnsdóttir, S.Ó.; Matter, J.M.; Stute, M.; Júlíusson, B.M.; et al. The rapid and cost-effective capture and subsurface mineral storage of carbon and sulfur at the CarbFix2 site. *Int. J. Greenh. Gas Con.* **2018**, *79*, 117–126. [[CrossRef](#)]
25. Hills, C.D.; Tripathi, N.; Carey, P.J. Mineralization technology for carbon capture, utilization, and storage. *Front. Energy Res.* **2020**, *8*, 142. [[CrossRef](#)]
26. Sandalow, D.; Aines, R.; Friedmann, J.; Kelemen, P.; McCormick, C.; Power, I.M.; Schmidt, B.; Wilson, S.A.S. *Carbon Mineralization Roadmap (ICEF Innovation Roadmap Project)*; Lawrence Livermore National Laboratory: California, USA, 2021.
27. Goff, F.; Lackner, K.S. Carbon dioxide sequestering using ultramafic rocks. *Environ. Geosci.* **1998**, *5*, 89–102. [[CrossRef](#)]
28. McGrail, B.P.; Schaeff, H.T.; Ho, A.M.; Chien, Y.J.; Dooley, J.J.; Davidson, C.L. Potential for carbon dioxide sequestration in flood basalts. *J. Geophys. Res. Solid Earth* **2006**, *111*, B12201. [[CrossRef](#)]

29. Styles, M.T.; Sanna, A.; Lacinska, A.M.; Naden, J.; Maroto-Valer, M. The variation in composition of ultramafic rocks and the effect on their suitability for carbon dioxide sequestration by mineralization following acid leaching. *Greenh. Gases Sci. Technol.* **2014**, *4*, 440–451. [[CrossRef](#)]
30. Mervine, E.M.; Wilson, S.; Power, I.M.; Dipple, G.M.; Turvey, C.C.; Hamilton, J.L.; Vanderzee, S.; Raudsepp, M.; Southam, C.; Matter, J.M.; et al. Potential for offsetting diamond mine carbon emissions through mineral carbonation of processed kimberlite: An assessment of De Beers mine sites in South Africa and Canada. *Mineral. Petrol.* **2018**, *112*, 755–765. [[CrossRef](#)]
31. Nisbet, H.; Buscarnera, G.; Carey, J.W.; Chen, M.A.; Detournay, E.; Huang, H.; Hyman, J.D.; Kang, P.K.; Kang, Q.; Labuz, J.F.; et al. Carbon mineralization in fractured mafic and ultramafic rocks: A review. *Rev. Geophys.* **2024**, *62*, e2023RG000815. [[CrossRef](#)]
32. Le Maitre, R.W.; Streckeisen, A.; Zanettin, B.; Le Bas, M.J.; Bonin, B.; Bateman, P. (Eds.) *Igneous Rocks: A Classification and Glossary of Terms: Recommendations of the International Union of Geological Sciences Subcommission on the Systematics of Igneous Rocks*, 2nd ed.; Cambridge University Press: Cambridge, UK, 2002.
33. Berner, R.A.; Lasaga, A.C.; Garrels, R.M. The carbonate-silicate geochemical cycle and its effect on atmospheric carbon dioxide over the past 100 million years. *Am. J. Sci.* **1983**, *283*, 641–683. [[CrossRef](#)]
34. Seifritz, W. CO₂ disposal by means of silicates. *Nature* **1990**, *345*, 486. [[CrossRef](#)]
35. Brady, P.V. The effect of silicate weathering on global temperature and atmospheric CO₂. *J. Geophys. Res. Solid Earth* **1991**, *96*, 18101–18106. [[CrossRef](#)]
36. Raymo, M.E.; Ruddiman, W.F. Tectonic forcing of late Cenozoic climate. *Nature* **1992**, *359*, 117–122. [[CrossRef](#)]
37. Berner, R.A.; Berner, E.K. Silicate weathering and climate. In *Tectonic Uplift and Climate Change*; Ruddiman, W.F., Ed.; Springer: Boston, MA, USA, 1997; pp. 353–365.
38. Gaillardet, J.; Dupré, B.; Louvat, P.; Allègre, C.J. Global silicate weathering and CO₂ consumption rates deduced from the chemistry of large rivers. *Chem. Geol.* **1999**, *159*, 3–30. [[CrossRef](#)]
39. Kelemen, P.B.; Hirth, G. Reaction-driven cracking during retrograde metamorphism: Olivine hydration and carbonation. *Earth Planet. Sci. Lett.* **2012**, *345–348*, 81–89. [[CrossRef](#)]
40. Beaulieu, E.; Goddérat, Y.; Donnadieu, Y.; Labat, D.; Roelandt, C. High sensitivity of the continental-weathering carbon dioxide sink to future climate change. *Nat. Clim. Change* **2012**, *2*, 346–349. [[CrossRef](#)]
41. Streit, E.; Kelemen, P.; Eiler, J. Coexisting serpentine and quartz from carbonate-bearing serpentized peridotite in the Samail Ophiolite, Oman. *Contribut. Mineral. Petrol.* **2012**, *164*, 821–837. [[CrossRef](#)]
42. Falk, E.S.; Kelemen, P.B. Geochemistry and petrology of listvenite in the Samail ophiolite, Sultanate of Oman: Complete carbonation of peridotite during ophiolite emplacement. *Geochim. Cosmochim. Acta* **2015**, *160*, 70–90. [[CrossRef](#)]
43. Penman, D.E.; Caves Rugenstein, J.K.; Ibarra, D.E.; Winnick, M.J. Silicate weathering as a feedback and forcing in Earth’s climate and carbon cycle. *Earth-Sci. Rev.* **2020**, *209*, 103298. [[CrossRef](#)]
44. Schuiling, R.D.; Krijgsman, P. Enhanced weathering: An effective and cheap tool to sequester CO₂. *Clim. Change* **2006**, *74*, 349–354. [[CrossRef](#)]
45. Hartmann, J.; West, A.J.; Renforth, P.; Köhler, P.; De La Rocha, C.L.; Wolf-Gladrow, D.A.; Dürr, H.H.; Scheffran, J. Enhanced chemical weathering as a geoengineering strategy to reduce atmospheric carbon dioxide, supply nutrients, and mitigate ocean acidification. *Rev. Geophys.* **2013**, *51*, 113–149. [[CrossRef](#)]
46. Moosdorf, N.; Renforth, P.; Hartmann, J. Carbon dioxide efficiency of terrestrial enhanced weathering. *Environ. Sci. Technol.* **2014**, *48*, 4809–4816. [[CrossRef](#)]
47. IPCC. *IPCC Special Report on Global Warming of 1.5 °C*; Cambridge University Press: Cambridge, UK, 2018.
48. Strelfer, J.; Amann, T.; Bauer, N.; Kriegler, E.; Hartmann, J. Potential and costs of carbon dioxide removal by enhanced weathering of rocks. *Environ. Res. Lett.* **2018**, *13*, 034010. [[CrossRef](#)]
49. Power, I.M.; Paulo, C.; Rausis, K. The mining industry’s role in enhanced weathering and mineralization for CO₂ removal. *Environ. Sci. Technol.* **2024**, *58*, 43–53. [[CrossRef](#)] [[PubMed](#)]
50. Taylor, L.L.; Quirk, J.; Thorley, R.M.S.; Kharecha, P.A.; Hansen, J.; Ridgwell, A.; Lomas, M.R.; Banwart, S.A.; Beerling, D.J. Enhanced weathering strategies for stabilizing climate and averting ocean acidification. *Nat. Clim. Change* **2016**, *6*, 402–406. [[CrossRef](#)]
51. Edwards, D.P.; Lim, F.; James, R.H.; Pearce, C.R.; Scholes, J.; Freckleton, R.P.; Beerling, D.J. Climate change mitigation: Potential benefits and pitfalls of enhanced rock weathering in tropical agriculture. *Biol. Lett.* **2017**, *13*, 20160715. [[CrossRef](#)]
52. Montserrat, F.; Renforth, P.; Hartmann, J.; Leermakers, M.; Knops, P.; Meysman, F.J. Olivine dissolution in seawater: Implications for CO₂ sequestration through enhanced weathering in coastal environments. *Environ. Sci. Technol.* **2017**, *51*, 3960–3972. [[CrossRef](#)]
53. Haque, F.; Santos, R.M.; Dutta, A.; Thimmanagari, M.; Chiang, Y.W. Co-benefits of wollastonite weathering in agriculture: CO₂ sequestration and promoted plant growth. *ACS Omega* **2019**, *4*, 1425–1433. [[CrossRef](#)] [[PubMed](#)]
54. Haque, F.; Santos, R.M.; Chiang, Y.W. CO₂ sequestration by wollastonite-amended agricultural soils—An Ontario field study. *Int. J. Greenh. Gas Con.* **2020**, *97*, 103017. [[CrossRef](#)]

55. Cong, L.; Lu, S.; Jiang, P.; Zheng, T.; Yu, Z.; Lü, X. CO₂ sequestration and soil improvement in enhanced rock weathering: A review from an experimental perspective. *Greenh. Gases Sci. Technol.* **2024**, *14*, 1122–1138. [CrossRef]
56. Medeiros, F.P.; Theodoro, S.H.; Carvalho, A.M.X.; Oliveira, V.S.; Oliveira, L.C.; Almeida, R.M.P.; Viana, M.B.; Gomide, C.S. The combination of crushed rock and organic matter enhances the capture of inorganic carbon in tropical soils. *J. S. Am. Earth Sci.* **2025**, *152*, 105254. [CrossRef]
57. Maroto-Valer, M.M.; Fauth, D.J.; Kuchta, M.E.; Zhang, Y.; AndréSEN, J.M. Activation of magnesium rich minerals as carbonation feedstock materials for CO₂ sequestration. *Fuel Process. Technol.* **2005**, *86*, 1627–1645. [CrossRef]
58. Power, I.M.; Dipple, G.M.; Bradshaw, P.M.D.; Harrison, A.L. Prospects for CO₂ mineralization and enhanced weathering of ultramafic mine tailings from the Baptiste nickel deposit in British Columbia, Canada. *Int. J. Greenh. Gas Con.* **2020**, *94*, 102895. [CrossRef]
59. Vienne, A.; Poblador, S.; Portillo-Estrada, M.; Hartmann, J.; Ijehon, S.; Wade, P.; Vicca, S. Enhanced weathering using basalt rock powder: Carbon sequestration, co-benefits and risks in a mesocosm study with *Solanum tuberosum*. *Front. Clim.* **2022**, *4*, 869456. [CrossRef]
60. Paulo, C.; Power, I.M.; Zeyen, N.; Wang, B.; Wilson, S. Geochemical modeling of CO₂ sequestration in ultramafic mine wastes from Australia, Canada, and South Africa: Implications for carbon accounting and monitoring. *Appl. Geochem.* **2023**, *152*, 105630. [CrossRef]
61. Taksavasu, T.; Arin, P.; Khatecha, T.; Kojinok, S. Microtextural characteristics of ultramafic rock-forming minerals and their effects on carbon sequestration. *Minerals* **2024**, *14*, 597. [CrossRef]
62. Barr, S.M.; Tantisukrit, C.; Yaowanoiyothin, W.; Macdonald, A.S. Petrology and tectonic implications of Upper Paleozoic volcanic rocks of the Chiang Mai belt, northern Thailand. *J. Southeast Asian Earth Sci.* **1990**, *4*, 37–47. [CrossRef]
63. DMR. *Geology of Thailand*, 1st ed.; Department of Mineral Resources, Ministry of Natural Resources and Environment: Bangkok, Thailand, 2014.
64. Metcalfe, I. Permian tectonic framework and palaeogeography of SE Asia. *J. Asian Earth Sci.* **2002**, *20*, 551–566. [CrossRef]
65. Phajuy, B.; Panjasawatwong, Y.; Osataporn, P. Preliminary geochemical study of volcanic rocks in the Pang Mayo area, Phrao, Chiang Mai, northern Thailand: Tectonic setting of formation. *J. Asian Earth Sci.* **2005**, *24*, 765–776. [CrossRef]
66. Bandibas, J.; Takarada, S. Geoinformation sharing system for East and Southeast Asia using SDI, OGC web services and FOSS. *Int. J. Geosci.* **2019**, *10*, 209–224. [CrossRef]
67. DMR. Geological Map of Thailand on 1:50,000 Scale. 2007. Available online: https://www.dmr.go.th/wp-content/uploads/2022/10/INDEXgeo50k_8_60-Model.pdf (accessed on 5 September 2024).
68. Promneewat, K.; Taksavasu, T.; Mankhemthong, N.; Siritongkham, N. Offline interactive map from hybrid app development: A case from geologic map app. In Proceedings of the 27th International Computer Science and Engineering Conference (ICSEC), Samui, Thailand, 14–15 September 2023; pp. 331–334.
69. DMR. Thailand WEBGIS Geoinformation System: Geoinformation Sharing System for East and Southeast Asia. Available online: <https://geohazards-info.gsj.jp/gsi/thailand/index.php> (accessed on 16 August 2024).
70. Koukouzas, N.; Koutsovitis, P.; Tyrologou, P.; Karkalis, C.; Arvanitis, A. Potential for mineral carbonation of CO₂ in Pleistocene basaltic rocks in Volos Region (Central Greece). *Minerals* **2019**, *9*, 627. [CrossRef]
71. Kwon, S. Mineralization for CO₂ Sequestration Using Olivine Sorbent in the Presence of Water Vapor. Ph.D. Thesis, Georgia Institute of Technology, Atlanta, GA, USA, 2011.
72. Rasool, M.H.; Ahmad, M. Reactivity of basaltic minerals for CO₂ sequestration via in situ mineralization: A review. *Minerals* **2023**, *13*, 1154. [CrossRef]
73. Garcia, B.; Beaumont, V.; Perfetti, E.; Rouchon, V.; Blanchet, D.; Oger, P.; Dromart, G.; Huc, A.Y.; Haeseler, F. Experiments and geochemical modelling of CO₂ sequestration by olivine: Potential, quantification. *Appl. Geochem.* **2010**, *25*, 1383–1396. [CrossRef]
74. Munz, I.A.; Brandvoll, Ø.; Haug, T.A.; Iden, K.; Smeets, R.; Kihle, J.; Johansen, H. Mechanisms and rates of plagioclase carbonation reactions. *Geochim. Cosmochim. Acta* **2012**, *77*, 27–51. [CrossRef]
75. Zevenhoven, R.; Slotte, M.; Koivisto, E.; Erlund, R. Serpentinite carbonation process routes using ammonium sulfate and integration in industry. *Energy Technol.* **2017**, *5*, 945–954. [CrossRef]
76. Daval, D.; Martinez, I.; Corvisier, J.; Findling, N.; Goffé, B.; Guyot, F. Carbonation of Ca-bearing silicates, the case of wollastonite: Experimental investigations and kinetic modeling. *Chem. Geol.* **2009**, *265*, 63–78. [CrossRef]
77. Gerdemann, S.J.; Dahlin, D.C.; O'Connor, W.K.; Penner, L.R.; Rush, G.E. Ex-situ and in-situ mineral carbonation as a means to sequester carbon dioxide. In Proceedings of the 21st Annual International Pittsburgh Coal Conference, Osaka, Japan, 13–17 September 2004; p. 17.
78. Zevenhoven, R.; Kavalaiskaite, I. Mineral carbonation for long-term CO₂ storage: An exergy analysis. *Int. J. Thermodyn.* **2004**, *7*, 23–31.
79. Monasterio-Guillot, L.; Fernandez-Martinez, A.; Ruiz-Agudo, E.; Rodriguez-Navarro, C. Carbonation of calcium-magnesium pyroxenes: Physical-chemical controls and effects of reaction-driven fracturing. *Geochim. Cosmochim. Acta* **2021**, *304*, 258–280. [CrossRef]

80. Olajire, A.A. A review of mineral carbonation technology in sequestration of CO₂. *J. Petrol. Sci. Eng.* **2013**, *109*, 364–392. [CrossRef]
81. Deer, W.A.; Howie, R.A.; Zussman, J. *Rock-Forming Minerals*, 2nd ed.; The Geological Society: London, UK, 1997.
82. Morimoto, N.; Fabries, J.; Ferguson, A.K.; Ginzburg, I.V.; Ross, M.; Seifert, F.A.; Zussman, J.; Aoki, K.; Gottardi, G. Nomenclature of pyroxenes. *Mineral. Mag.* **1998**, *52*, 535–550. [CrossRef]
83. Ding, W.; Fu, L.; Ouyang, J.; Yang, H. CO₂ mineral sequestration by wollastonite carbonation. *Phys. Chem. Miner.* **2014**, *41*, 489–496. [CrossRef]
84. Min, Y.; Li, Q.; Voltolini, M.; Kneafsey, T.; Jun, Y.S. Wollastonite carbonation in water-bearing supercritical CO₂: Effects of particle size. *Environ. Sci. Technol.* **2017**, *51*, 13044–13053. [CrossRef]
85. Yan, Y.; Dong, X.; Li, R.; Zhang, Y.; Yan, S.; Guan, X.; Yang, Q.; Chen, L.; Fang, Y.; Zhang, W.; et al. Wollastonite addition stimulates soil organic carbon mineralization: Evidences from 12 land-use types in subtropical China. *Catena* **2023**, *225*, 107031. [CrossRef]
86. Lackner, K.S. Carbonate chemistry for sequestering fossil carbon. *Annu. Rev. Energy Environ.* **2002**, *27*, 193–232. [CrossRef]
87. Cao, X.; Li, Q.; Xu, L.; Tan, Y. Experiments of CO₂-basalt-fluid interactions and micromechanical alterations: Implications for carbon mineralization. *Energy Fuels* **2024**, *38*, 6205–6214. [CrossRef]
88. Wu, J.C.S.; Sheen, J.-D.; Chen, S.-Y.; Fan, Y.-C. Feasibility of CO₂ fixation via artificial rock weathering. *Ind. Eng. Chem. Res.* **2001**, *40*, 3902–3905. [CrossRef]
89. Wang, F.; Dreisinger, D.; Jarvis, M.; Hitchins, T. Kinetic evaluation of mineral carbonation of natural silicate samples. *Chem. Eng. J.* **2021**, *404*, 126522. [CrossRef]
90. Wilson, S.; Dipple, G.M.; Power, I.M.; Barker, S.L.; Fallon, S.J.; Southam, G. Subarctic weathering of mineral wastes provides a sink for atmospheric CO₂. *Environ. Sci. Technol.* **2011**, *45*, 7727–7736. [CrossRef]
91. Amann, T.; Hartmann, J.; Hellmann, R.; Pedrosa, E.T.; Malik, A. Enhanced weathering potentials—The role of in situ CO₂ and grain size distribution. *Front. Clim.* **2022**, *4*, 929268. [CrossRef]
92. Stubbs, A.R.; Paulo, C.; Power, I.M.; Wang, B.; Zeyen, N.; Wilson, S. Direct measurement of CO₂ drawdown in mine wastes and rock powders: Implications for enhanced rock weathering. *Int. J. Greenh. Gas Con.* **2022**, *113*, 103554. [CrossRef]
93. Reershemius, T.; Kelland, M.E.; Jordan, J.S.; Davis, I.R.; D’Ascanio, R.; Kalderon-Asael, B.; Asael, D.; Suhrhoff, T.J.; Epihov, D.Z.; Beerling, D.J.; et al. Initial validation of a soil-based mass-balance approach for empirical monitoring of enhanced rock weathering rates. *Environ. Sci. Technol.* **2023**, *57*, 19497–19507. [CrossRef]
94. Lewis, A.L.; Sarkar, B.; Wade, P.; Kemp, S.J.; Hodson, M.E.; Taylor, L.L.; Yeong, K.L.; Davies, K.; Nelson, P.N.; Bird, M.I.; et al. Effects of mineralogy, chemistry and physical properties of basalts on carbon capture potential and plant-nutrient element release via enhanced weathering. *Appl. Geochem.* **2021**, *132*, 105023. [CrossRef]
95. Renforth, P. The potential of enhanced weathering in the UK. *Int. J. Greenh. Gas Con.* **2012**, *10*, 229–243. [CrossRef]
96. Lefebvre, D.; Goglio, P.; Williams, A.; Manning, D.A.C.; de Azevedo, A.C.; Bergmann, M.; Meersmans, J.; Smith, P. Assessing the potential of soil carbonation and enhanced weathering through Life Cycle Assessment: A case study for Sao Paulo State, Brazil. *J. Clean. Prod.* **2019**, *233*, 468–481. [CrossRef]
97. Beerling, D.J.; Kantzas, E.P.; Lomas, M.R.; Wade, P.; Eufrasio, R.M.; Renforth, P.; Sarkar, B.; Andrews, M.G.; James, R.H.; Pearce, C.R.; et al. Potential for large-scale CO₂ removal via enhanced rock weathering with croplands. *Nature* **2020**, *583*, 242–248. [CrossRef]
98. Zhou, Q. Potential CO₂ capture via enhanced weathering by basaltic sand spreading on golf courses in the U.S. *Int. J. Greenh. Gas Con.* **2024**, *131*, 104032. [CrossRef]
99. Kelland, M.E.; Wade, P.W.; Lewis, A.L.; Taylor, L.L.; Sarkar, B.; Andrews, M.G.; Lomas, M.R.; Cotton, T.E.A.; Kemp, S.J.; James, R.H.; et al. Increased yield and CO₂ sequestration potential with the C4 cereal Sorghum bicolor cultivated in basaltic rock dust-amended agricultural soil. *Glob. Change Biol.* **2020**, *26*, 3658–3676. [CrossRef] [PubMed]
100. Vanderkloot, E.; Ryan, P. Quantifying the effect of grain size on weathering of basaltic powders: Implications for negative emission technologies via soil carbon sequestration. *Appl. Geochem.* **2023**, *155*, 105728. [CrossRef]
101. Power, I.M.; Hatten, V.N.J.; Guo, M.; Schaffer, Z.R.; Rausis, K.; Klyn-Hesselink, H. Are enhanced rock weathering rates overestimated? A few geochemical and mineralogical pitfalls. *Front. Clim.* **2025**, *6*, 1510747. [CrossRef]
102. Harrison, A.L.; Dipple, G.M.; Power, I.M.; Mayer, K.U. Influence of surface passivation and water content on mineral reactions in unsaturated porous media: Implications for brucite carbonation and CO₂ sequestration. *Geochim. Cosmochim. Acta* **2015**, *148*, 477–495. [CrossRef]
103. Jerden, J.; Mejbel, M.; Filho, A.N.Z.; Carroll, M.; Campe, J. The impact of geochemical and life-cycle variables on carbon dioxide removal by enhanced rock weathering: Development and application of the Stella ERW model. *Appl. Geochem.* **2024**, *167*, 106002. [CrossRef]

Disclaimer/Publisher’s Note: The statements, opinions and data contained in all publications are solely those of the individual author(s) and contributor(s) and not of MDPI and/or the editor(s). MDPI and/or the editor(s) disclaim responsibility for any injury to people or property resulting from any ideas, methods, instructions or products referred to in the content.